Structures 71 (2025) 107954

Contents lists available at ScienceDirect

Structures

journal homepage: www.elsevier.com/locate/structures

Hybrid Discrete-Finite Element method for biaxially-discretized structures

Igor Bouckaert [a,*], Michele Godio [b], João Pacheco de Almeida [a]

[a] Institute of Mechanics, Materials and Civil Engineering (iMMC), UCLouvain, Place du Levant 2, Louvain-la-Neuve, 1348, Belgium
[b] RISE Research Institutes of Sweden, Brinellgatan 4, Borås, 504 62, Sweden

ARTICLE INFO

Keywords:
Discrete elements
Finite elements
Hybrid models
Coupled models
Contact
Discontinuities
Saint-Venant
Frames
Block structures
Walls

ABSTRACT

The HybriDFEM method, short for Hybrid Discrete-Finite Element Method, combines both discrete and finite element approaches in a single numerical model: the method adopts a discrete representation of the structure, but the formulation is designed to integrate continuous parts that can be simulated by the Finite Element Method, allowing hybrid numerical mock-ups to be built. The scope of application of the method is expanded from its original development for uniaxially-discretized (1D) structures to modeling biaxially-discretized (2D) structures and systems of beams connected through rigid-node connections. The possibility to integrate finite elements within HybriDFEM in 2D is initially formalized. A two-step contact detection algorithm, in which the interface detection is preceded by a preliminary rough detection, is then presented. Finally, different approaches to modeling contact are introduced, depending on whether it is meant to reflect the behavior of a continuous material, flexible interfaces, or point-wise contact. These new capabilities of the 2D HybriDFEM method are validated on a series of selected examples including solutions from analytical models, classical finite elements, and limit analysis; among others, the HybriDFEM method is used to evaluate the axial and shear stress distribution in a linear elastic beam with negligible error relative to analytical solutions, and to predict the collapse load of in-plane loaded masonry frames with an error below 0.05% compared to solutions from limit analysis. The adequacy of the method to enhance discrete simulations by integrating finite elements is illustrated in a conclusive example via the pushover analysis of a flexible masonry frame.

1. Introduction

Numerical modeling has become an indispensable tool in the structural analysis of buildings and infrastructure, providing engineers with a powerful means to assess their response and optimize their design. In response to the demand for reliable structural predictions, a vast collection of numerical models has been proposed in the literature, with two modeling approaches being typically distinguished [1,2]: discrete and continuous. While discrete models are idealizations in which material regions are separate and their interaction is represented explicitly, in continuous models, heterogeneity is smeared into an equivalent medium [3] and their interaction is only invoked by means of homogenized constitutive laws [4]. Each approach has its own strengths and limitations [5], and is more or less suited for specific structural typologies. Using only one of these approaches to simulate the response of large structures can therefore be challenging due to the limitations they bring: among other, limited accuracy in modeling discontinuities and strong nonlinearities by continuous models [6], and prohibitive computational cost by discrete ones.

To address this challenge, hybrid (or coupled) models can be developed by integrating discrete and continuous approaches within a single numerical mock-up, leveraging their respective strengths. The selection of the appropriate formulation allows for the efficient modeling of each structural component, with discontinuity-governed components utilizing a discrete approach, and others making use of a more computationally efficient continuous approach. However, creating hybrid models is not a straightforward task, as it requires careful considerations on the computational framework and solution strategy to adopt for the discrete and continuous parts of the model, and the interface across said parts. Such approaches have been applied to model granular media [7,8] or solids [9,10].

In Bouckaert et al. [11], the Hybrid Discrete-Finite Element method, or in short HybriDFEM, was introduced for the modeling of uniaxially-discretized (1D) members like beams and columns. The HybriDFEM method adopts a discrete representation of the structure by explicitly modeling each individual building block and its interactions with neighboring elements. The method allows nonlinear contact, as well as large block displacements and rotations to be described. More importantly, the formulation is designed to integrate continuous parts that are modeled by the Finite Element Method (FEM), allowing hybrid numerical mock-ups to be built.

* Corresponding author.
E-mail address: igor.bouckaert@uclouvain.be (I. Bouckaert).

https://doi.org/10.1016/j.istruc.2024.107954
Received 30 July 2024; Received in revised form 27 November 2024; Accepted 28 November 2024
Available online 18 December 2024

In this paper, the HybriDFEM method presented in Bouckaert et al. (2024) [11] is extended to biaxially-discretized (2D) structures. It starts by introducing rigid node connections to enable the link between multiple unaligned 1D members, allowing 2D systems of beams to be modeled (trusses, frames, etc.). The rigid connections also enable the coupling of HybriDFEM blocks to classical FEM elements in 2D. More importantly, building upon the mathematical developments presented for 1D members [11], the HybriDFEM method is herein extended to 2D discretizations, considerably broadening the range of applicability of the method to 2D structural components with embedded discontinuities (e.g., masonry walls) and micro-structured materials.

Formulations that explicitly represent discontinuities in 2D structures have been proposed since the late 1970s; see, among the others, the Discrete Element Method (DEM), used for, e.g., granular media [12] or masonry structures [13,14]. However, these formulations usually require a time-stepping solution algorithm, which considerably increases the computational burden when used to solve quasi-static problems [15]. More recently, discrete modeling approaches like the Rigid Body Spring Model [16,17], the Rigid Block model [18,19], and the Applied Element Method (AEM) [20–22], proposed a discrete spring-block representation of the structure, making use of more affordable solution schemes.

Approaches that model discontinuities with the Finite Element Method (FEM) have been developed over the years. These approaches can model discontinuities as an equivalent continuum [23–25] or 'spread' them over a certain area [26], thereby not enabling their precise location. Obtaining an equivalent continuum can be achieved through homogenization techniques, which were developed, e.g., for masonry [27–29] or reinforced concrete [30–32]. Other approaches include discontinuities directly in the mesh; if the location of the discontinuity is known a priori, predefined cracks can be introduced by making use of, e.g., zero-length interface elements [33–35] or boundary elements [36]. If the location of the discontinuity is unknown, remeshing strategies have been proposed to gradually adapt the mesh to the emergence of discontinuities [37,38]. Methods like the eXtended Finite Element Method (X-FEM) propose a formulation in which the discontinuity is introduced via discontinuous fields, making it independent of the mesh [39,40]. FE approaches that use a very refined mesh to explicitly describe the discontinuity, referred to as micro-modeling approaches [41], also appear in the literature [42–44]. Although accurate, these methods are not suitable for modeling large structures due to their prohibiting cost. Mixed FEM/DEM numerical methods enable the inclusion of deformable elements within a discrete element framework. While these methods are precise, they are too costly and therefore not suitable for modeling large structures within a realistic time frame [45–47]. Idealizations like the Macro-Distinct Element Model (M-DEM) [48] were built upon this method and combined with homogenization techniques to alleviate this issue.

The HybriDFEM method falls under the category of discrete modeling approaches, with the noticeable additional features that it uses multiple springs in series at the block interfaces and that discrete parts can be coupled with FEs, representing continuous parts, and leading to hybrid models. This special feature makes the present formulation suitable for modeling large structures, while also being capable of modeling discontinuities.

In Bouckaert et al. [11], all the examples presented consisted of aligned blocks and, consequently, a number of interfaces linearly dependent on the number of blocks. The extension of HybriDFEM to 2D leads to block arrangements that increase in complexity: blocks can extend along both planar axes and be misaligned, and the number of interfaces can drastically increase. This highlights the need for an automated detection of block interfaces. Contact detection is a key aspect in discrete modeling, as it can considerably affect the performance of the model [49]. This is especially true in the context of contact formulations that involve finite sliding [50–52], according to which contact pairs must be updated at each time step. The suitability of one contact detection algorithm over another strongly depends on the nature of the problem and on the shape of the building blocks that are in contact [53]. The proprietary software UDEC [54] adopts a contact detection algorithm based on the 'common plane' approach, which deforms as two adjacent blocks come into contact [55,56]. Other contact detection algorithms, such as the open source software LMGC90 [57,58], detect contact in two consecutive phases, the first based on a rough approximation of the block shape called 'bounding box', and the second, more accurate, based on the real block shape and performed only on the adjacent blocks resulting from phase 1 [59,60]. Other methods to improve the efficacy of contact detection, especially suitable for large and sparse particle assemblies, are based on the spatial decomposition of the problem [61]. In this paper, a novel algorithm is implemented for contact detection between quadrilateral HybriDFEM blocks, which starts by detecting potential contact based on the smallest enclosing circle (SEC) of the blocks, then proceeding edge by edge to identify those that overlap. In this study, the HybriDFEM is tested on 2D structures composed of relatively few dense blocks (few hundreds). Moreover, a small-sliding formulation is adopted in HybriDFEM, with contact pairs being detected at the beginning of the analysis only. For this reason, the detection algorithm described here prioritizes simplicity of implementation over computational efficacy. Its performance is largely sufficient for the examples currently handled.

Most of the discrete formulations found in the literature resort to edge-to-edge point-wise contact representations, be it for modeling rocks [62], masonry structures [63], or grains [64]. Two approaches are classically distinguished: convex approaches, in which the interaction between building blocks occurs through one single contact point, usually located at the center of the interface, and concave approaches, where the interaction is distributed on multiple points. The contact properties are defined accordingly, with the former approach being analytically more challenging to define because it requires the definition of the interface's bending behavior, while the latter, although costlier, is based on the assumption that two primary types of forces are exchanged: normal and tangential [65,66]. The HybriDFEM method adopts a concave approach [11], with contact points modeled by pairs of nonlinear 2D springs in series. In Bouckaert et al. [11], the mechanical properties of the springs were deduced by attributing a specific material volume (or area in 2D) to each spring and scaling the assumed material stress–strain relationship accordingly. This approach is similar to the one used in AEM [67]. Although it serves well as a proxy for modeling continuous structures, it is less ideal for simulating assemblies of rigid blocks that interact through deformable interfaces. In UDEC, which also adopts an edge-to-edge point-wise contact representation, a contact area (or length in 2D) is attributed to each specific contact point, and the contact constitutive model relates the contact stress with the displacement jump [68,69]. In LMGC90, the contact constitutive model relates the contact force transmitted through each point to its displacement, without associating it with a particular contact length [70]. This force–displacement approach is occasionally used in UDEC to model, e.g., reinforcements [54]. In this paper, HybriDFEM's contact modeling capabilities are extended to offer the possibility to model contact by the three above-mentioned descriptions: a force–displacement relationship similar to LMGC90's, a stress–displacement relationship similar to UDEC's, and a stress–strain relationship similar to AEM's, already adopted in [11]. This extension provides great versatility in modeling contacts and, as highlighted by the examples presented in this article, allows for the coverage of a wide range of structural typologies.

The objective of the present study is to extend the scope of HybriDFEM to structures other than the uniaxially-discretized beams and columns previously studied, particularly 2D structures such as masonry walls, frames, or in general, biaxially-discretized members. This is described in Section 2 along with the computational framework needed to couple HybriDFEM to FEM elements. The extension to 2D is facilitated by the introduction of a contact detection algorithm, presented in

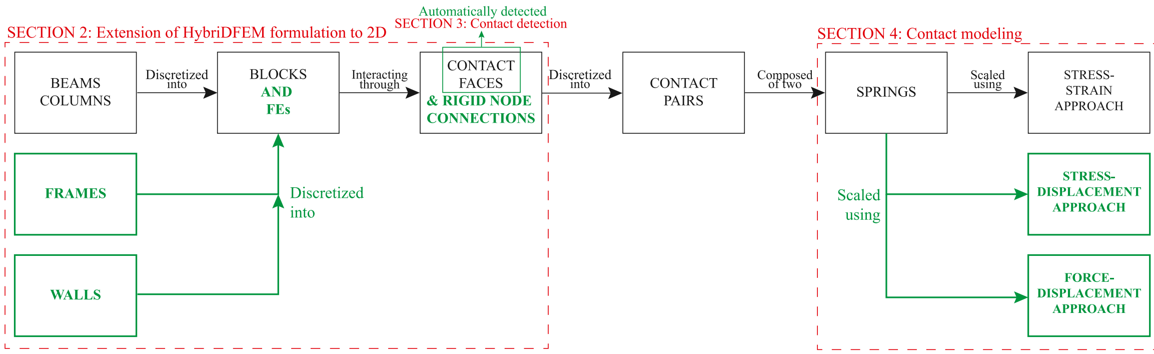

Fig. 1. Flowchart presenting additional features of HybriDFEM introduced in the present paper, in green. The manuscript sections describing each additional feature are indicated in red.

Section 3. In Section 4, new possibilities are offered to model block interactions by proposing various ways to define the constitutive laws governing contact, depending on the specificity of the structure under study.

In Section 5, a series of validation examples are put forward to show the described novelties and assess the accuracy of HybriDFEM, both for systems of beams and 2D structures. Given the method's current stage of early development, those examples were selected primarily for their simplicity and the possibility of obtaining analytical or numerical solutions that are straightforward to interpret and compare with results from HybriDFEM. First, The stress–strain approach is validated against the analytical solution for the axial and shear stress distributions of a continuous linear elastic beam. It is shown how, contrary to the 1D solution [11], Saint Venant's effects can be captured by the herein proposed 2D formulation. The rigid node connections and a new elastoplastic material that includes residual deformations are validated through an application example consisting of a frame subjected to cyclic loading. The capability of HybriDFEM to model the response of 2D discrete systems, including their pre- and post-peak behavior, which shows itself challenging when using other discrete modeling approaches [15,71], is highlighted by a pushover analysis on a dry-stacked masonry wall. The performance of HybriDFEM's contact detection algorithm is then demonstrated by computing the pushover curve of masonry frames and comparing it with the solution obtained by limit analysis taken from the literature. A final illustrative example showcases HybriDFEM's capability to integrate classical FEM elements within the mock-up, leading to nonlinear hybrid frame models.

2. HybriDFEM for biaxially-discretized structures

According to the HybriDFEM method [11], the structure is discretized into rigid blocks, which are regular and quadrilateral. They are not necessarily aligned, and their size varies. The interaction between two rigid blocks in contact is described by a Contact Face (CF), which is deformable and in turn discretized into a series of Contact Pairs (CPs), which is made of two nonlinear springs in series. An edge-to-edge point-wise contact description is adopted, meaning that contact occurs across the CFs. This also includes vertex-to-edge contact configurations as the limit case.

All these components were mathematically described in the previous work [11] in which HybriDFEM was used to model uniaxially-discretized elements (columns and beams). In this section and the following ones, several important additions are made at various levels to extend the method's scope to 2D structures. The flowchart in Fig. 1 provides a simplified representation of how HybriDFEM is structured. The elements shown in black represent components introduced previously, while those in green correspond to the extensions discussed in this paper, with their corresponding section indicated in red.

2.1. Block discretization

The strategy adopted for block discretization is user-defined and depends strongly on the nature of the problem at hand. For instance, when modeling beam-like members, the discretization is performed along the longitudinal axis only [11]. With the developments introduced in the current paper for HybriDFEM 2D, however, it is possible for the adopted block discretization to match the structural stereotomy [72,73]. Fig. 2 shows two examples of simple 2D structures modeled with HybriDFEM: on the left, a frame composed of two HybriDFDEM beam-like block-assembled members and a beam finite element, connected via rigid node connections at the corners; on the right, a block discretization reproducing the stereotomy of a masonry wall.

In a general case, the structure is discretized into n_b rigid blocks. The three degrees of freedom (DoFs) of a generic block i, or group of rigidly connected blocks, are U_{3i-2}, U_{3i-1} and U_{3i}. They are collected in the vector of global displacements $\mathbf{U} \in \mathbb{R}^{3n_b}$, and describe the kinematics of the block at its reference origin in the global reference system (X, Y). The DoFs of the two example structures are represented in red in Fig. 2.

In some application examples presented in this paper, a rigid node connection between two blocks is performed similarly to what is done in classical FE codes. By linking the local DoFs of the two blocks that are connected with the same global DoFs through appropriate connectivity matrices [11,74], the kinematics of the two blocks will be identical at the structural level.

2.2. Contact faces

The block discretization results in n_{CF} contact faces (CFs). While the algorithm developed to automatically detect CFs is described in Section 3.1, the convention used to define CFs and pairs of blocks that are in contact is as follows.

Consider two generic adjacent blocks, later denoted as block A and block B (Fig. 3). Numerically, two nodes are needed to describe the geometry and orientation of their CF: the block vertices delimiting the CF, whose coordinates are $\mathbf{x}_{e1}$ and $\mathbf{x}_{e2}$. The unit vector $\hat{\mathbf{e}}_{CF}$ describing the direction of the CF is:

$$\hat{\mathbf{e}}_{CF} = \frac{\mathbf{x}_{e2} - \mathbf{x}_{e1}}{||\mathbf{x}_{e2} - \mathbf{x}_{e1}||}, \tag{1}$$

where $||\cdot||$ is the vector norm, thus $||\mathbf{x}_{e2} - \mathbf{x}_{e1}||$ equals the CF length. The unit vector $\hat{\mathbf{n}}_{CF}$,

$$\hat{\mathbf{n}}_{CF} = \begin{bmatrix} 0 & -1 \\ 1 & 0 \end{bmatrix} \hat{\mathbf{e}}_{CF}, \tag{2}$$

is perpendicular to $\hat{\mathbf{e}}_{CF}$ and is used to establish the orientation of the CF, as well as the convention used to distinguish the two blocks: $\hat{\mathbf{n}}_{CF}$ points from block B to block A.

Once blocks A and B are identified, the coordinates of their reference origins, expressed in the global reference system, are stored in

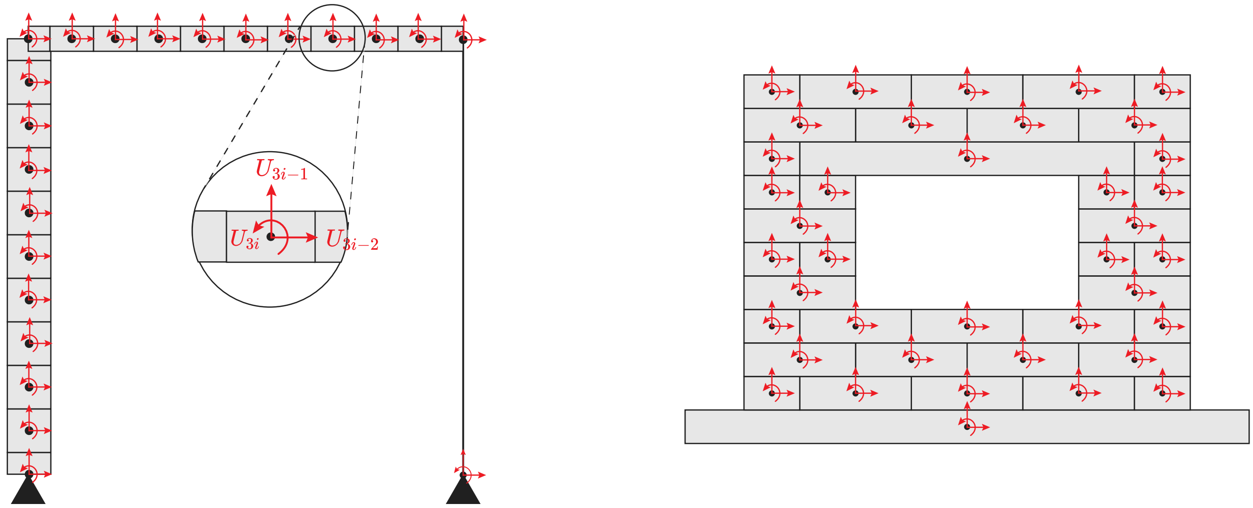

Fig. 2. Continuous frame modeled by coupling HybriDFEM and FEM (left) and masonry wall modeled with HybriDFEM (right).

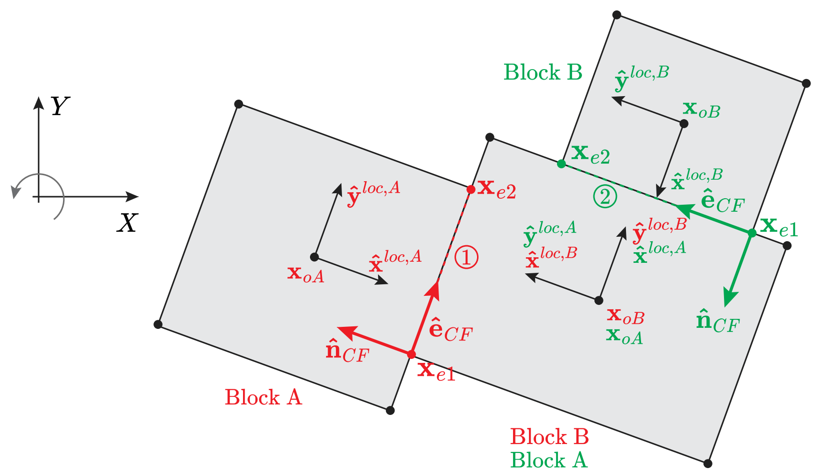

Fig. 3. Convention used for contact faces and block pairs in HybriDFEM 2D. The nomenclature relative to CF 1 is indicated in red, the one relative to CF 2 is in green.

the vectors $\mathbf{x}_{oA}$ and $\mathbf{x}_{oB}$, respectively, and two local coordinate systems $(x^{loc,A}, y^{loc,A})$ and $(x^{loc,B}, y^{loc,B})$ are attached to their reference origins, with their unit vectors being noted $\hat{\mathbf{x}}^{loc,A}$, $\hat{\mathbf{y}}^{loc,A}$, $\hat{\mathbf{x}}^{loc,B}$, and $\hat{\mathbf{y}}^{loc,B}$. For both local coordinate systems, the x-axis is perpendicular to the CF and points toward it, while the y-axis is parallel and in the same direction as $\hat{\mathbf{e}}_{CF}$.

The kinematics of a CF is described by 6 DoFs in the global reference system, corresponding to the kinematics of the adjacent blocks A and B, which are stored in the vector $\mathbf{q}_f^{glob} \in \mathbb{R}^6$ (Fig. 4). Namely, a connectivity matrix, sometimes also referred to as localization matrix, $\mathbf{A}_f$ is attributed to each CF to link the DoF $\mathbf{q}_f^{glob}$ of one CF with the ones of the structures, $\mathbf{U}$ [11], as expressed below. The resisting forces of the structure, $\mathbf{P}_r$, as well as its stiffness matrix $\mathbf{K}$, are assembled from the resisting forces $\mathbf{p}_f^{glob}$ and stiffness matrices $\mathbf{k}_f^{glob}$ of each CF, expressed in the global reference system:

$$\begin{aligned}\mathbf{q}_f^{glob} &= \mathbf{A}_f\mathbf{U}\\ \mathbf{P}_r &= \sum \mathbf{A}_f^T\mathbf{p}_f^{glob}\\ \mathbf{K} &= \sum \mathbf{A}_f^T\mathbf{k}_f^{glob}\mathbf{A}_f.\end{aligned} \tag{3}$$

2.3. Contact pair discretization

Contact occurs point-wise, through n_{CP} contact pairs (CPs) distributed along each CF. In Section 3.3, different strategies for CP discretizations are discussed. In what follows, the definition of the CP is given.

A contact pair consists of three points, A, B, and C. Points A and B are fixed on the corresponding blocks (Fig. 4). Two bidirectional springs in series connect point A with point B. The orientation of these two springs follows the orientation of the corresponding blocks. The springs are connected through the intermediate, hinged point C [11]. In the undeformed configuration, the three points coincide. The position $\mathbf{x}_{CP_i}$ of the three coinciding points A, B and C of a generic CP i in the undeformed configuration can be determined:

$$\mathbf{x}_{CP_i} = \mathbf{x}_{e1} + \left(i - \frac{1}{2}\right) \cdot h_{CP} \cdot \hat{\mathbf{e}}_{CF}, \tag{4}$$

where $h_{CP} = \frac{||\mathbf{x}_{e2}-\mathbf{x}_{e1}||}{n_{CP}}$ is the distance between CPs determined by the chosen CF discretization. It is important to note that this equation pertains to a uniform distribution of CPs along the CF, typically when HybriDFEM is used as a proxy for continuous structures. In that case, the distance between the first CP and the edge of the CF is $h_{CP}/2$. However, some application examples require the CPs to be placed either on the edge or at a specific distance from the edge of the CF. This aspect is discussed in Section 3.3, in which other possible CP distributions are described.

The quantities ℓ_{Ax} and ℓ_{Ay} (Fig. 4), required to derive the kinematics of one CP from the kinematics of its CF [11], describe the relative

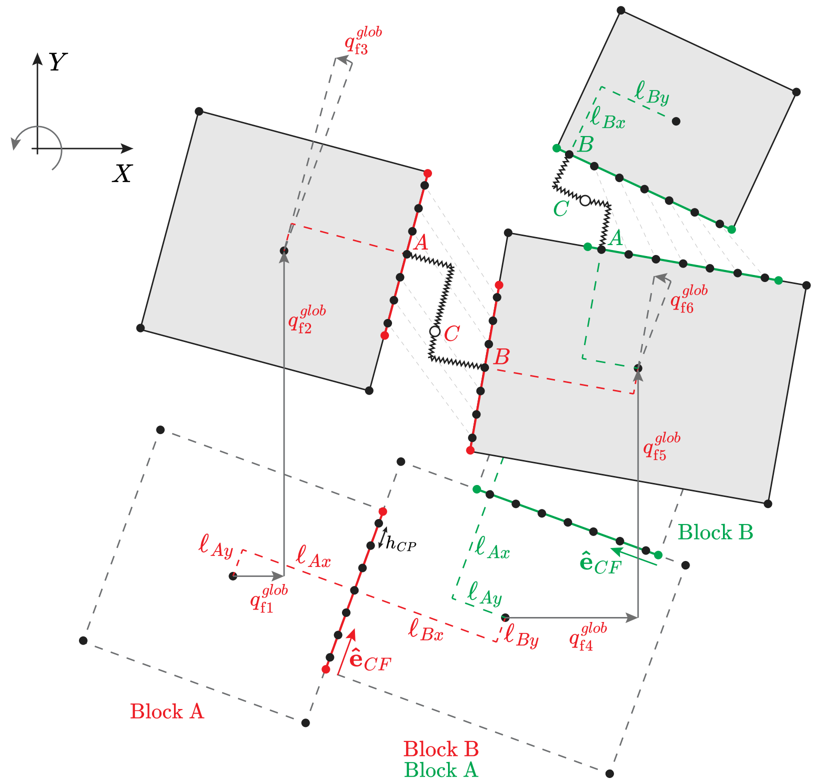

Fig. 4. Two contact faces between three blocks in their undeformed (dashed lines) and deformed (solid lines) configurations. On the deformed configuration, one CP is highlighted on each CF.

position of point A with respect to the reference origin of the block A:

$$\ell_{Ax} = \left(\mathbf{x}_{CP_i} - \mathbf{x}_{oA}\right) \cdot \hat{\mathbf{x}}^{loc,A}$$
$$\ell_{Ay} = \left(\mathbf{x}_{CP_i} - \mathbf{x}_{oA}\right) \cdot \hat{\mathbf{y}}^{loc,A}, \tag{5}$$

and similarly for the quantities ℓ_{Bx} and ℓ_{By}, which describe the relative position of point B with respect to the reference origin of block B:

$$\ell_{Bx} = \left(\mathbf{x}_{CP_i} - \mathbf{x}_{oB}\right) \cdot \hat{\mathbf{x}}^{loc,B}$$
$$\ell_{By} = \left(\mathbf{x}_{CP_i} - \mathbf{x}_{oB}\right) \cdot \hat{\mathbf{y}}^{loc,B}. \tag{6}$$

Since the blocks are rigid, said quantities are constants.

The kinematics of a contact pair is therefore described by the kinematics of the three points (two translations and one rotation for points A and B, and two translations for point C) and it is stored in the vector $\mathbf{q}^c \in \mathbb{R}^8$. Since the orientations of blocks A and B can differ, it is convenient to express $\mathbf{q}^c$ in the global coordinate system (X, Y, Z) [11].

2.4. Geometric nonlinearity

The HybriDFEM method captures geometric nonlinearities by means of a co-rotational formulation capable of accurately modeling large block displacements and rotations [11].

Taking into account the large rigid-body motion of the blocks, the first six DoFs of the CP, q_1^c to q_6^c, depend non-linearly on the six DoFs of their contact face [11], and the last two DoFs, q_7^c and q_8^c, corresponding to the kinematics of point C, are initially unknown as they depend on the properties of the springs, as described in Section 2.5.

Upon exclusion of the rigid-body motions of the blocks, the vector $\mathbf{q}^c$ can be condensed into only four basic coordinates, indicated with $\mathbf{q}^{bsc} \in \mathbb{R}^4$, thus reducing the number of DoFs to describe each CP and the associated computational cost. This vector contains the relative motion of point A with respect to point B, and the orientation of the two bidirectional springs [11]. These basic quantities are needed to describe the deformation of the CP and are derived from $\mathbf{q}^c$ through linear relations. The effects of geometric nonlinearities are captured by establishing equilibrium of the CP in the deformed configuration [11].

2.5. Material nonlinearity

The HybriDFEM method also accounts for material nonlinearities. In [11], contact constitutive laws were assigned to the springs by scaling the constitutive law of the material composing the corresponding blocks. In this article, different ways of defining contact laws are explored (Section 4).

The basic coordinates $\mathbf{q}^{bsc}$ of the CP do not include information on the relative deformations ΔL_{An}, ΔL_{As}, ΔL_{Bn} and ΔL_{Bs}, which correspond to the normal and tangential elongations of the two springs, respectively ΔL_n and ΔL_s, and are stored in the vector $\mathbf{\Delta} L = \left[\Delta L_n \quad \Delta L_s\right]^T$.

The calculation of the relative elongations, and consequently the calculation of the position of point C, is based on compatibility and equilibrium equations, whose variables are illustrated in Fig. 5. For two springs connected in series, compatibility ensures that the sum of the spring elongations is equal to the total elongation of the CP. On the other hand, equilibrium imposes equality on the two bidirectional spring forces. The compatibility equations are linear while the equilibrium equations can be nonlinear, depending on the constitutive relations of the springs (Section 4), which relate their elongations $\mathbf{\Delta} L$ to their respective forces $\mathbf{F}_{\text{spring}} = \left[F_n \quad F_s\right]^T$.

2.6. Internal solution procedure

The set of compatibility and equilibrium equations is solved by means of an iterative nonlinear solution procedure, referred to as 'internal solution procedure'.

In [11], a classical Newton–Raphson procedure was used for said procedure, requiring the tangent stiffness matrix of the spring's force–elongation relationship. In this paper, an additional powerful nonlinear solution procedure has been implemented, to deal with cases where

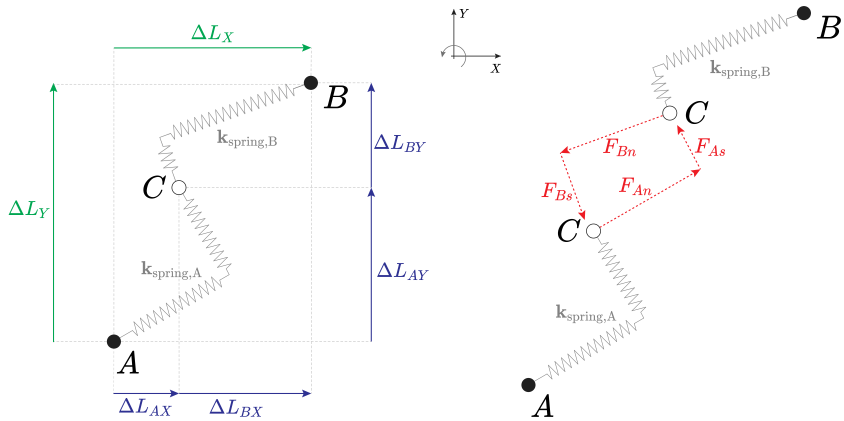

Fig. 5. Kinematic (left) and static (right) unknowns of the two springs in series composing the contact pair [73].

the Newton–Raphson method is not able to achieve convergence after a user-defined number of steps. In particular, the program uses Powell's conjugate direction method to find the root of the given set of equations. As this method does not require the use of derivatives of the mathematical function for which a solution is sought [75], it is better suited when evaluation of the tangent stiffness matrix results in an ill-conditioned matrix. This method has proven useful, for example, for obtaining the response of columns in post-buckling [76,77], which could not be obtained using the internal Newton–Raphson procedure alone.

2.7. External solution procedure

The internal solution procedure is nested within the nonlinear 'external solution procedure', common to all nonlinear FE methods, which is applied at the structural level. To do so, a solution scheme was developed in [11]. The road-map illustrating said scheme is shown in dashed lines in Fig. 6.

The external solution procedure makes use of an implicit solver, which, similarly to what is classically done in FEM codes, solves a system of equations that involve both current and next values of the unknowns in the time-stepping approach. In this framework, it finds the set of global displacements $\mathbf{U}$ for which the corresponding structural resisting forces $\mathbf{P}_r$ are in equilibrium with the applied forces $\mathbf{P}_{ref}$. At each increment i, the applied forces are scaled by a factor λ_i which is controlled either by a force-controlled, displacement-controlled, or work-controlled procedure [78].

Computing the tangent stiffness matrix of the structure at each iteration of the procedure enables achieving quadratic convergence. If said matrix cannot be inverted and convergence cannot be achieved, a modified Newton–Raphson method making use of the initial stiffness matrix is used to the price of losing quadratic convergence.

2.8. Coupling with finite elements

HybriDFEM shares similarities with both the DE and FE methods. Although the adopted formulation is discrete, the procedure applied to compute the resisting force vector $\mathbf{P}_r$ from the displacement vector $\mathbf{U}$ is identical to the implicit nonlinear solution schemes used in FE codes (Fig. 6). This attribute allows integrating HybriDFEM with FEs, which is performed by summing the local contributions of each type of element to the global resisting forces of the structure.

As for the rigid node connections between blocks, FEs are connected to blocks, or other FEs, via one of their nodes, by coupling their kinematics. In presence of rigid node connections and FEs, the total number of DoFs of a 2D HybriDFEM structure at the global level becomes, instead of n_b, $n_{DoF} = 3(n_b + n_{\text{FE}} - n_r)$, where n_{FE} is the number of FE nodes and n_r is the total number of rigid connections between blocks and/or FEs.

As an illustration for this feature, a 6-DoF linear elastic beam FE is used, which accounts for large displacements through a co-rotational formulation. In its undeformed configuration, the element is straight and forms an angle θ with the X-axis. The procedure described below is illustrated in blue lines in Fig. 6.

As for the HybriDFEM, a localization matrix $\mathbf{A}_{\text{FE}} \in \mathbb{R}^{6\times n_{DoF}}$ is used to extract the DoFs of the structure that correspond to the local DoFs $\mathbf{q}_{\text{FE}}^{glob} \in \mathbb{R}^6$ of the finite element:

$$\mathbf{q}_{\text{FE}}^{glob} = \mathbf{A}_{\text{FE}}\mathbf{U}, \tag{7}$$

which is then expressed in a coordinate system aligned with the orientation of the element in its undeformed configuration (also known as local reference system):

$$\mathbf{q}_{\text{FE}}^{loc} = \mathbf{T}_{\text{FE}}(\theta) \cdot \mathbf{q}_{\text{FE}}^{glob}, \tag{8}$$

where $\mathbf{T}_{\text{FE}}(\theta)$ is a rotation matrix. Finally, using a 'co-rotational' (or basic) reference system that follows the motion of the beam element, three basic displacements $\mathbf{q}_{\text{FE}}^{bsc}$ of the FE are derived, excluding the rigid-body motion of the element. A common choice for the basic coordinates of a beam are the chord elongation and the chord rotations at both extremities [79,80], but other basic coordinate systems are possible.

In the absence of material nonlinearities, the resisting forces $\mathbf{p}_{\text{FE}}^{bsc}$ of the element can be derived from its basic displacements and stiffness matrix:

$$\mathbf{p}_{\text{FE}}^{bsc} = \mathbf{k}_{\text{FE}}^{bsc} \cdot \mathbf{q}_{\text{FE}}^{bsc}, \tag{9}$$

where the expression of $\mathbf{k}_{\text{FE}}^{bsc}$ varies from one FE formulation to the other. Numerous expressions exist in the literature for, e.g., Euler–Bernoulli FEs [80–82], or Timoshenko FEs [83–85]. The formulation described in [83] is used in the illustration example presented in Section 5.5

From the basic resisting forces, the local and global resisting forces $\mathbf{p}_{\text{FE}}^{loc}$ and $\mathbf{p}_{\text{FE}}^{glob}$ can be derived successively by expressing equilibrium in the deformed configuration and then changing the coordinates to the global system. Finally, the global resisting forces of the structure are obtained by assembling the contributions of all CFs and FEs, amending Eq. (3):

$$\mathbf{P}_r = \sum_{CFs} \mathbf{A}_{\text{f}}^T \mathbf{p}_{\text{f}}^{glob} + \sum_{FEs} \mathbf{A}_{\text{FE}}^T \mathbf{p}_{\text{FE}}^{glob}. \tag{10}$$

Similarly, the tangent stiffness matrix $\mathbf{K}$ of the structure is assembled using the local stiffness matrices of all CFs and FEs composing the structure.

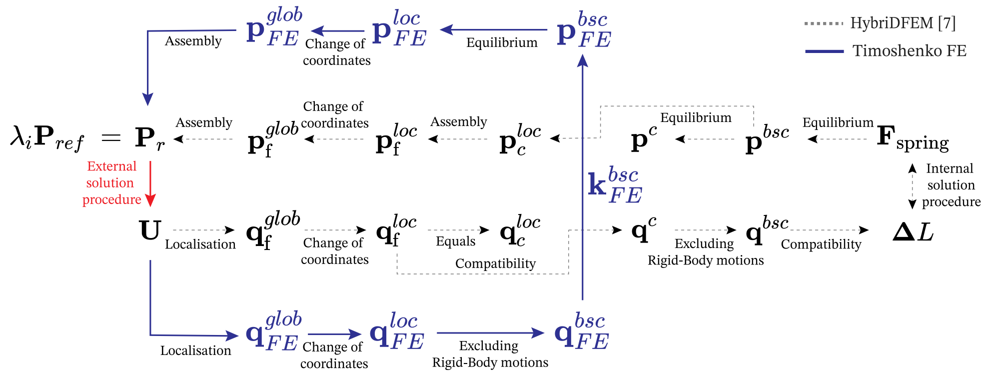

Fig. 6. Road-map for assembling the global resisting forces from a given set of global displacements, both for HybriDFEM (dashed lines) [11] and for a Timoshenko FE (blue lines). At each step, the corresponding tangent stiffness matrix is assembled.

The above procedure described for a simple linear beam element can be extrapolated to more complex FEM formulations, such as those accounting for nonlinear material effects, or FEs other than beams.

3. Contact detection

The 2D HybriDFEM formulation can deal with quadrilateral blocks that can differ in size and orientation. Adjacent blocks communicate at their interfaces by an edge-to-edge point-wise contact representation. Point-wise contact implies that interactions occur at specific points of the CF, denoted as CPs (Section 2). A small-sliding contact formulation is adopted in HybriDFEM, which implies that contact is detected only at the beginning of the simulation, on the initial configuration.

This section discusses new features implemented in the HybriDFEM framework, namely the contact detection algorithm (Section 3.1), deletion and recovery of contacts (Section 3.2), and possible strategies for CP discretization (Section 3.3).

3.1. Contact detection algorithm

The contact detection algorithm operates block-pairwise, assessing the presence of a contact face between two neighboring blocks for all consecutive pairs of potentially interacting blocks. For each pair of blocks, the algorithm defines a candidate block and an antagonist block (nomenclature borrowed from [86]). Numerically, the geometry of a block is described by 5 nodes. Four represent the vertices of the block and are ordered such that two successive nodes are connected by an edge. The fifth corresponds to the reference origin of the block, not necessarily coinciding with its center of mass. Prior to running the contact detection algorithm, the center and radius of the smallest enclosing circle (SEC) of all the blocks are computed using Welzl's algorithm [87]. When looping through the block pairs, if the candidate and antagonist blocks' SECs intersect, the block pair is considered for potential contact and the algorithm computes the equation of the four lines describing the block edges in the form $Ax+By+C=0$ (Fig. 7). For a generic edge delimited by vertices (x_1, y_1) and (x_2, y_2), the equation's coefficients write:

$$A = \frac{y_2 - y_1}{x_2 - x_1} \quad , \qquad B = -1 \qquad \text{and} \qquad C = y_1 - Ax_1. \tag{11}$$

If $(x_2 - x_1)$ becomes too close to zero within a given tolerance, the line is considered to be vertical, which yields $A = 1$, $B = 0$ and $C = -x_1$.

This procedure returns four triplets $(A, B, C)_{1,2,3,4}$ for both the candidate and antagonistic block. The resulting triplets are compared and, if an identical triplet is found within a given tolerance, the vertices of the corresponding edges are sorted along the common line to check if blocks overlap. To do so, it is sufficient to sort the sum of the vertices' x- and y-coordinates in ascending order. Designating the sorted vertices of the candidate block as n_{11} and n_{12} and those of the antagonist block as n_{21} and n_{22}, five distinct cases are possible depending on their relative arrangement (Fig. 8): no overlap (Case 1); partial overlap of block 1 over block 2 (Case 2); full overlap of block 1 over block 2 (Case 3), or inversely (Cases 4 and 5). If contact is detected (i.e., all cases except Case 1), the algorithm returns the two nodes delimiting the CF. As described in Section 2.2, said nodes are used to create the CF along with the reference origins of the two adjacent blocks.

Algorithm 1 Contact detection.

```
Start with block i ⇐ 0
for i in 1, ..., n_b − 1 do
    for j in i + 1, ..., n_b do
        if Blocks i and j are rigidly connected (identical DoFs) then
            skip
        else if SEC of blocks i and j intersect then
            Pairwise detection between blocks i and j:
            Compute the four (A, B, C)_1,2,3,4 triplets for both blocks
            if Candidate and antagonist block have an identical triplet then
                Sort vertices of candidate and antagonist block: n_11, n_12, n_21, n_22
                if n_12 ≥ n_21 or n_22 ≥ n_11 then      ▷ No contact detected
                    skip
                else                                    ▷ Contact detected
                    return (min(n_11, n_21), max(n_12, n_22))
                    Create CF with block A ⇐ block i and block B ⇐ block j
                end if
            end if
        else skip
        end if
    end for
end for
```

Alg. 1 formalizes the above described procedure of block-pairwise contact detection, as it is implemented in HybriDFEM. The algorithm checks intersection of SECs for all possible pairs of blocks. This results in $\frac{n_b(n_b-1)}{2}$ checks for n_b blocks, i.e., the number of checks increases quadratically with n_b. However, since the operation performed during this preliminary step is computationally less expensive than the effective interface detection, it already allows for a drastic reduction in the computational time required for contact detection.

3.2. Contact deletion and recovery

HybriDFEM is unable to create new contact pairs or change the existing ones during the simulation. Contact can, nonetheless, be deleted when a specific criterion on the relative displacement or contact force is met at the CP. This covers cases where, for example, a large gap opens between the blocks or the tensile strength of the spring is reached.

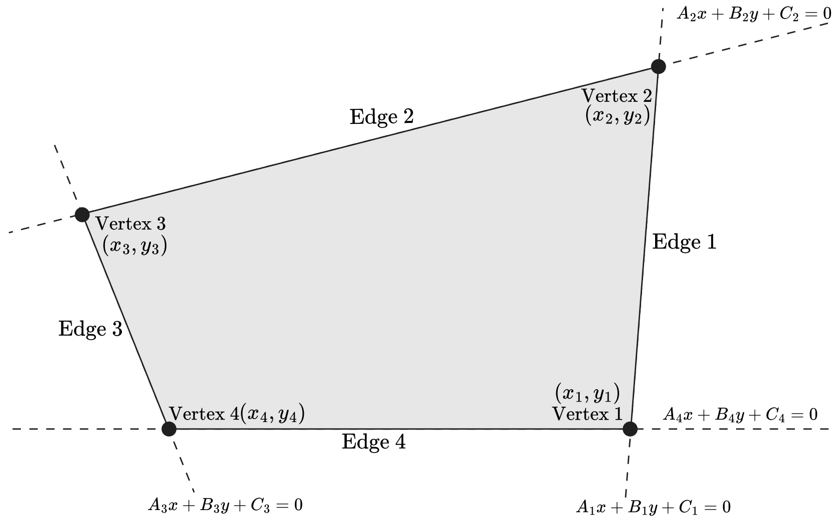

Fig. 7. Line equations describing the four edges of a block.

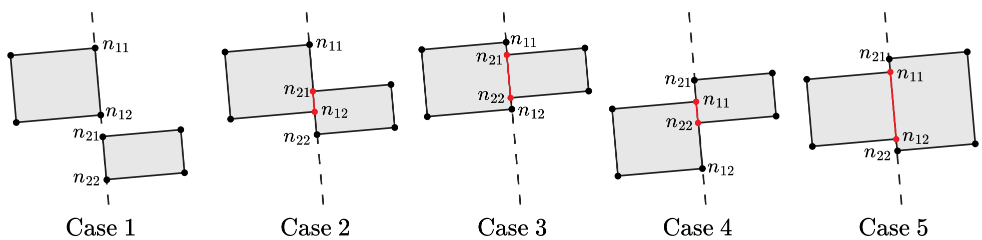

Fig. 8. Possible contact situations between the candidate and antagonist block (see Alg. 1).

Contact is deleted by operating an additional check on the CP at each time step, upon convergence of the internal solution procedure, i.e., when the forces and elongation of the two springs are known. Upon deletion, the contribution of the CP stops being included in the assembly of the global resisting forces and stiffness matrix. Deleting the CP does not, however, necessarily prevent its reactivation in a later stage of the simulation. Indeed, even if the contribution of the deleted CP to the resisting forces is overlooked, the additional check is still performed and can detect if the criterion for deletion is no longer met, and reactivate the CP accordingly. This allows for the simulation of scenarios involving the successive openings and closings of gaps (contact recovery).

3.3. Strategies for CP discretization

Fig. 9 illustrates the various ways provided by HybriDFEM to discretize the CFs. By default, a newly created CF is divided into n_{CP} uniformly distributed CPs, ensuring a uniform point-wise approximation of the contact stress distribution along the CF. However, strategically positioning the CPs based on prior knowledge of the expected structural behavior allows for an informed reduction of the number of CPs. To address these situations, a corner distribution (with and without offset) can be performed.

This is particularly important when modeling, e.g., dry-stacked masonry, where blocks undergo sliding and rocking, and stress concentrations can occur at the corners of the blocks. A very fine CP discretization would be necessary to capture it. On the other hand, minimizing the number of CPs helps decreasing the computational time, because it eliminates a nonlinear internal solution procedure per CP at each global iteration step, and it reduces the number of assembly operations to be performed when the resisting forces and tangent stiffness of the structure are computed, which occurs also at each iteration of the external solution procedure. When trying to reduce the number of CPs per CF, the choice to distribute them uniformly is no longer suitable, as the distance between the extremity of the CF and the CP that is closest to it becomes too large, and capturing the concentration of stresses at the corners is therefore unfeasible. In these cases, a corner distribution with only two CPs per CF can be performed. Said configuration allows reproducing closely the rocking behavior of the block, even if this is accompanied by a loss of precision in the stress distribution [88,89]. Additionally, an assumption frequently made when modeling dry masonry with DEM concerns the concentration of damage at the corners of the blocks, often taken into account by rounding off the corners of the blocks [15]. An equivalent approach can be applied with HybriDFEM by introducing an offset of the two CPs with respect to the extremity of the CF.

4. Contact modeling

The HybriDFEM method serves multiple simulation approaches [11]. On the one hand, it can be used to explicitly model existing structural discontinuities (masonry joints, cracks, soil–structure interactions, etc.). On the other, it proves to be an effective way to model continuous structures, potentially with embedded discontinuities, e.g., with the block interfaces representing potential crack planes. Additionally, it enables the integration of FEs, making it possible to build hybrid models.

While in the first case it can be convenient to model the interaction between the blocks directly by means of point-wise stress–displacement or force–displacement relationships, in the second case scaling laws can be used in the definition of the contact properties to asymptotically reproduce the material behavior [11]. These three different point-wise contact modeling approaches (force–displacement, stress–displacement, or stress–strain) are implemented in HybriDFEM, and can be used in the same model for different CFs, e.g., when modeling

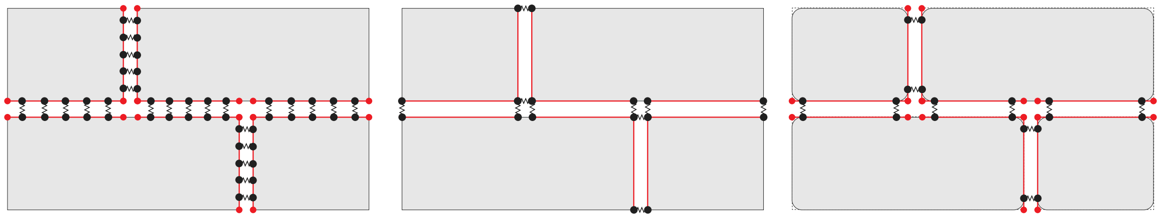

Fig. 9. Strategies for CP discretization offered in HybriDFEM: uniform and corner distributions, with or without offset.

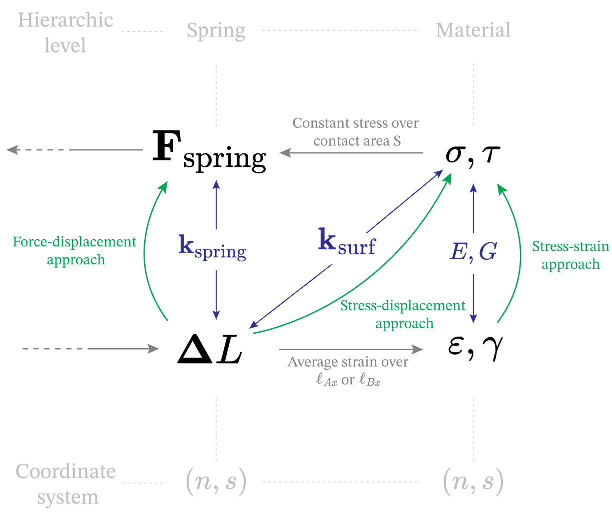

Fig. 10. Implementation of different contact modeling approaches in HybriDFEM.

a flexible column made of a continuous material lying on a rigid base [11].

As discussed next, for the force–displacement approach, the road-map shown in Fig. 6 applies (Section 4.1). When using the stress–strain (Section 4.2) or stress–displacement approach (Section 4.3), as shown in Fig. 10, an additional structural level is required, and the procedure to find the spring elongations and forces must be extended to the level of the stresses and/or strains.

4.1. Force–displacement approach

With this approach, the spring constitutive relation is provided, relating the spring elongations $\boldsymbol{\Delta L}$ to its forces $\mathbf{F}_{\text{spring}}$. When dealing with a nonlinear constitutive law, the tangent stiffness matrix of each of the two springs in series is required to achieve quadratic convergence both in the internal and external nonlinear solution procedures. Said matrix is referred to as $\mathbf{k}_{\text{spring}}$ and can be derived from the spring constitutive law as [11]:

$$\mathbf{k}_{\text{spring}} := \begin{bmatrix} k_{nn} & k_{ns} \\ k_{sn} & k_{ss} \end{bmatrix} = \begin{bmatrix} \frac{\partial F_n}{\partial \Delta L_n} & \frac{\partial F_n}{\partial \Delta L_s} \\ \frac{\partial F_s}{\partial \Delta L_n} & \frac{\partial F_s}{\partial \Delta L_s} \end{bmatrix}, \tag{12}$$

where the off-diagonal terms reflect the coupling between the normal and tangential behavior due to, e.g., interface dilatancy.

A typical example of application of this approach concerns the modeling of blocks in contact via vertex-to-edge or vertex-to-vertex contacts, representing, e.g., cases of block tilting. The spring law discussed below provides an illustration of such force–displacement approach, which was used in one of the validation examples (Section 5.3).

Example: Coulomb friction law

One example of a force–displacement law that has been implemented in HybriDFEM is the Amontons–Coulomb friction law [90], illustrated in Fig. 11. The parameters of the law are the following:

- The tensile strength of the spring F_y;
- The friction angle ϕ, and the corresponding friction coefficient $\mu = \tan\phi$;
- The cohesion c, corresponding to the shear strength when the normal force is 0;
- The normal and tangential stiffnesses of the spring k_{nn} and k_{ss}, respectively.

In the normal direction, the force–displacement relation is elastic in compression with stiffness k_{nn} and infinite compressive strength. In tension, the elastic branch is delimited by a tension cutoff at the maximal tensile force F_y, and the residual tensile strength is 0. The maximal tensile force is also used as the threshold for the contact deletion condition as described in Section 3.2, therefore deleting also the tangential component when the tension cutoff is reached. In the tangential direction, the force–displacement relation is an elastic-perfectly plastic law. No coupling between normal and tangential behavior is considered for this law, therefore $k_{ns} = k_{sn} = 0$.

4.2. Stress–strain approach

In this approach, a material constitutive law is provided, relating the material strains with material stresses. Scaling laws are necessary at two different steps during the internal solution procedure: linking strains to spring elongations, and stresses to spring forces. When modeling a continuous material, the deformation of the springs represents the average deformation of the portion of block that is associated to it, which has dimensions $b \times h_{CP} \times \ell_x$, where ℓ_x either stands for ℓ_{Ax} or ℓ_{Bx} and $S := b \times h_{CP}$ corresponds to the contact surface area associated to the CP.

From the spring elongations, the average axial and shear strains ε and γ on the corresponding portion of block are derived [11]:

$$\varepsilon = \frac{\Delta L_n}{\ell_x} \qquad \gamma = \frac{\Delta L_s}{\ell_x}. \tag{13}$$

The axial and shear stresses σ and τ are derived from the strains via the material constitutive relations, following which the spring forces can be recovered assuming that the stress is constant over the associated portion of the block:

$$F_n = \sigma \cdot S \qquad F_s = \tau \cdot S. \tag{14}$$

The incremental relation between the spring elongation and spring forces, corresponding to $\mathbf{k}_{\text{spring}}$, is derived from the incremental relation between strains and stresses:

$$\begin{aligned} k_{nn} &= \frac{\partial F_n}{\partial \Delta L_n} = \frac{\partial(\sigma S)}{\partial(\varepsilon \ell_x)} = \frac{S}{\ell_x} \cdot \frac{\partial \sigma}{\partial \varepsilon} \\ k_{ss} &= \frac{\partial F_s}{\partial \Delta L_s} = \frac{\partial(\tau S)}{\partial(\gamma \ell_x)} = \frac{S}{\ell_x} \cdot \frac{\partial \tau}{\partial \gamma}. \end{aligned} \tag{15}$$

In all the material models currently implemented in HybriDFEM, the axial stress does not depend on shear strains, and inversely, therefore the resulting stiffness matrix is diagonal.

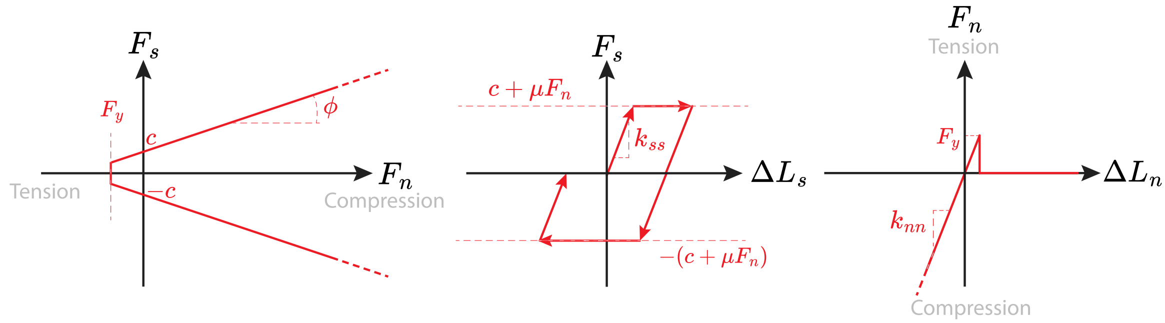

Fig. 11. Failure domain and force–displacement relations for the Amontons–Coulomb spring law with tension cutoff.

If the stress–strain law is linear, Eq. (15) simplifies to:

$$k_{nn} = \frac{S}{\ell_x} \cdot E$$
$$k_{ss} = \frac{S}{\ell_x} \cdot G, \tag{16}$$

where E is the material's Young's modulus and $G = E/(2(1+\nu))$ is the shear modulus. If the distribution of the shear stresses cannot be captured accurately, as was the case for 1D HybriDFEM [11], a shear correction factor χ, typically $(6+5\nu)/(5(1+\nu))$ for beams [91], is used on the shear stiffness parameter. However, as will be shown in Section 5.1, in 2D HybriDFEM the distribution of shear stresses is calculated with sufficient accuracy, and a correction factor is not necessary.

4.3. Stress–displacement approach

This contact modeling approach aligns with the approach traditionally employed in, e.g., UDEC [54], relating the stress to the spring elongation. This approach can prove useful when the CFs represent flexible, dimensionless mortar joints between rigid blocks.

In that case, a CF is subdivided into n_{CP} contact pairs, and the force in the spring is derived assuming constant stress over its associated contact area S, as is done for the stress–strain approach. The difference between the two approaches lies in the fact that, since the CF represents the behavior of a dimensionless joint rather than a portion of material, the elongation of the spring effectively represents the deformation of the joint at that point, and is not an average of the strains in a corresponding portion of the block, which is considered rigid.

As was done for the other approaches, the incremental relations between the contact stresses and spring elongations are necessary for the nonlinear solution procedure. From the stress–displacement constitutive law, the stiffness matrix $\mathbf{k}_{\text{surf}}$, representing the incremental relation between the stresses on the contact area and the spring elongation, can be derived:

$$\mathbf{k}_{\text{surf}} = \begin{bmatrix} k_{\sigma n} & k_{\sigma s} \\ k_{\tau n} & k_{\tau s} \end{bmatrix} = \begin{bmatrix} \frac{\partial \sigma}{\partial \Delta L_n} & \frac{\partial \sigma}{\partial \Delta L_s} \\ \frac{\partial \tau}{\partial \Delta L_n} & \frac{\partial \tau}{\partial \Delta L_s} \end{bmatrix}. \tag{17}$$

From there, the incremental relation for the scaled springs can be derived knowing that $F_n = \sigma \cdot S$ and $F_s = \tau \cdot S$, therefore:

$$\mathbf{k}_{\text{spring}} = \mathbf{k}_{\text{surf}} \cdot S. \tag{18}$$

The terms of the tangent stiffness matrix related to the surface law are all given in N/m^3, whereas the parameters of the tangent stiffness matrix related to the equivalent spring law are given in N/m.

5. Validation examples

Five examples are presented to illustrate the new possibilities offered by the extension of HybriDFEM to systems of beams and 2D structures. Some of the examples consist of continuous structures in which the stress–strain approach is adopted, others consist of assemblies of discrete blocks and adopt a force–displacement approach. In all examples, the contact detection algorithm described in Section 3 was applied at the start of the simulation and successfully detected the interfaces between the blocks.

5.1. Stress distribution in elastic beams

The first numerical example consists of a linear elastic cantilever beam, with a rectangular cross-section of dimensions $h \times b = 0.5$ m $\times$ 0.2 m, which is subjected to a vertical downwards force $F = 100$ kN at its free end. The beam is made of a continuous material, therefore a stress–strain approach as described in Section 4.2 is adopted with a linear elastic material characterized by $E = 30$ GPa and $\nu = 0$.

This example was already investigated with a block discretization performed along the longitudinal axis of the beam [11]. It yielded accurate results in terms of deflection and axial stress distribution. However, the shear stress distribution could not be captured because the discretization did not allow for shear stresses to develop inside the element in the direction parallel to the longitudinal axis of the beam, resulting in a constant distribution of stresses along the beam height.

The beam is now discretized longitudinally and transversely into a series of square blocks. Bearing in mind the shear span of the beam, which is equal to six, a transversal discretization in n_h blocks and a longitudinal discretization in $6n_h$ blocks was adopted, resulting in a total of $n_b = 6n_h^2$ blocks and $18n_h^2$ DoFs at the global level. All the detected CFs are further subdivided into n_{CP} CPs uniformly distributed across the CF. The boundary conditions are applied by blocking the three DoFs of all the leftmost blocks whilst the load F is uniformly distributed on all the rightmost blocks of the beam.

The results obtained with HybriDFEM are compared in terms of distributions of axial and shear stresses in the leftmost section of the beam, i.e. in its fixed end. For the axial stresses, beam theory indicates that the expected distribution is linear with $\sigma = 36$ MPa and $\sigma = -36$ MPa in the uppermost and lowest material fiber, respectively. On the other hand, Zhuravskii formula [92] indicates a quadratic shear stress distribution with null shear stress at the extreme top and bottom fibers and a maximal shear stress $\tau_{max} = \frac{3V}{2A} = 1.5$ MPa at the center of the section, where $V = 100$ kN is the shear force in the section and $A = 0.1$ m^2 is its cross-section.

This example is tested for different values of n_h and n_{CP}. Fig. 12 shows the axial and shear stresses in the beam along with its deflected shape, magnified by a factor 20, for a coarse and a fine mesh discretization, $n_h = 3 \times n_{CP} = 2$ and $n_h = 15 \times n_{CP} = 20$ respectively. Fig. 13 depicts the distribution of the axial and shear stresses in the leftmost section of the beam. The stresses obtained with HybriDFEM are represented in a blue bar graph, where each bar represents the stress in one CP. Due to the fineness of the discretization, the bars in the two graphs corresponding to the fine discretization are difficult to distinguish from one another.

Fig. 14 presents the shear stress distributions at the beam end regions, using the finest discretization, for two cases: when the vertical

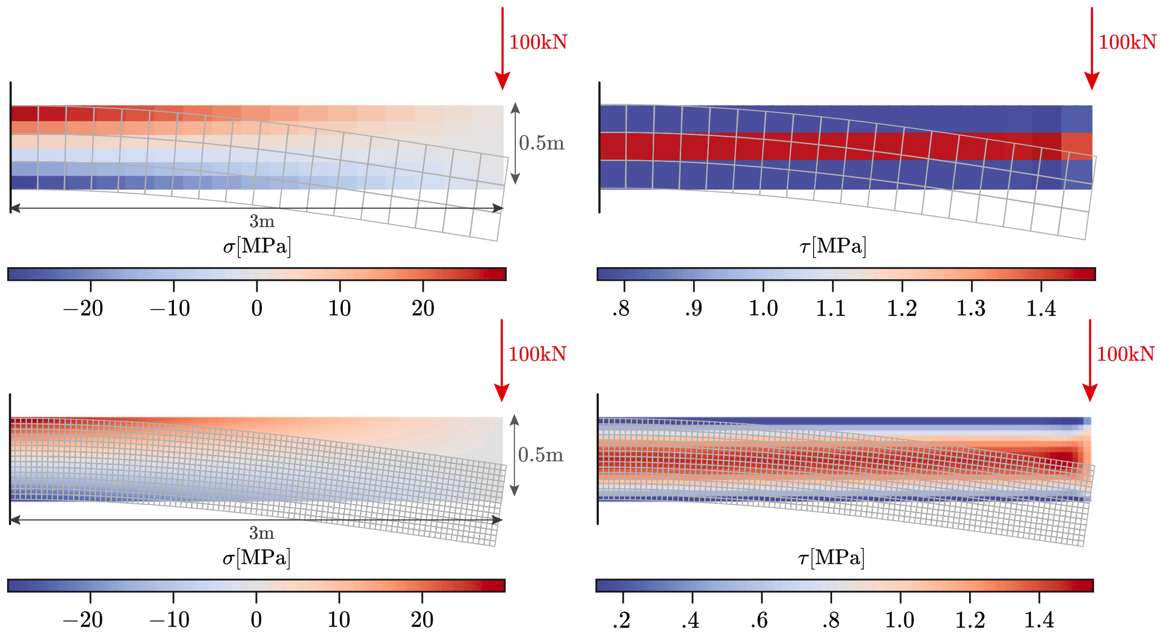

Fig. 12. Axial and shear stress distribution, and deformed shape of the beam with coarse ($n_h = 3$ and $n_{CP} = 2$) and fine ($n_h = 15$ and $n_{CP} = 20$) discretization.

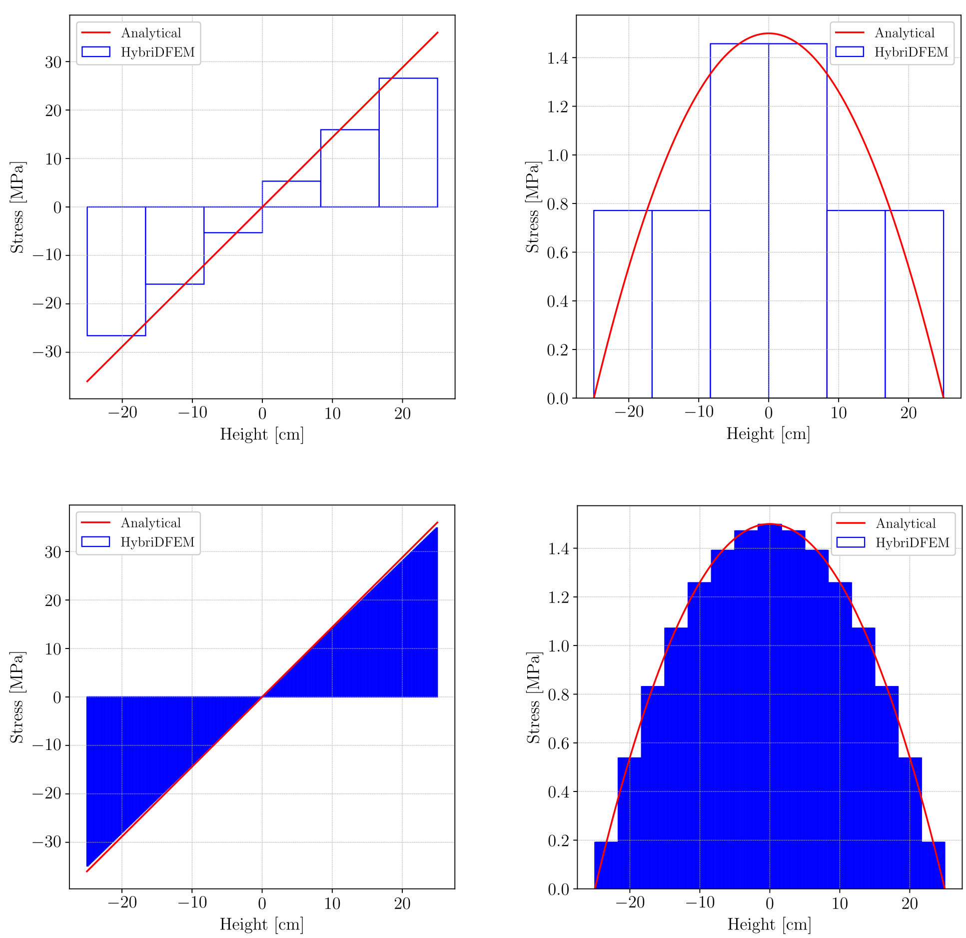

Fig. 13. Axial (left) and shear (right) stress distribution in the leftmost beam section (i.e. at the fixed support) for the coarse (top) and fine (bottom) beam discretizations.

downward force is applied on the upper right block, and when it is uniformly distributed across the blocks along the beam's height. The figure shows that the beam biaxial discretization enables Saint-Venant's principle to be illustrated with HybriDFEM: indeed, at a certain distance from the beam end, the difference between the shear stress distributions for both load cases becomes imperceptible.

The results of a convergence study are shown in Fig. 15, which is performed to assess the influence of the block and CP discretizations on

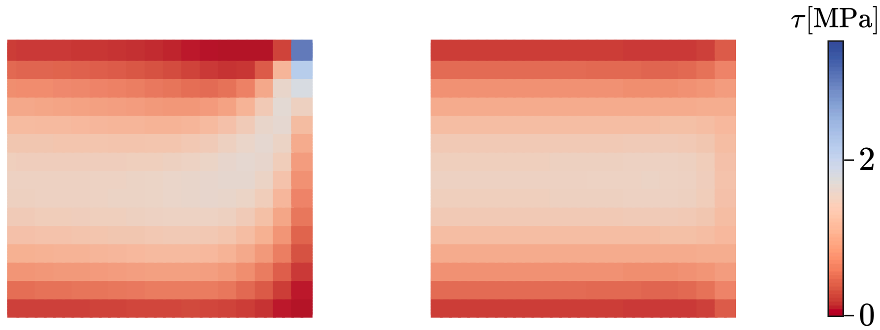

Fig. 14. Shear stress distributions at the beam end region for a vertical downward load applied on the upper right block (left) and uniformly distributed along the beam's height across all the rightmost blocks (right).

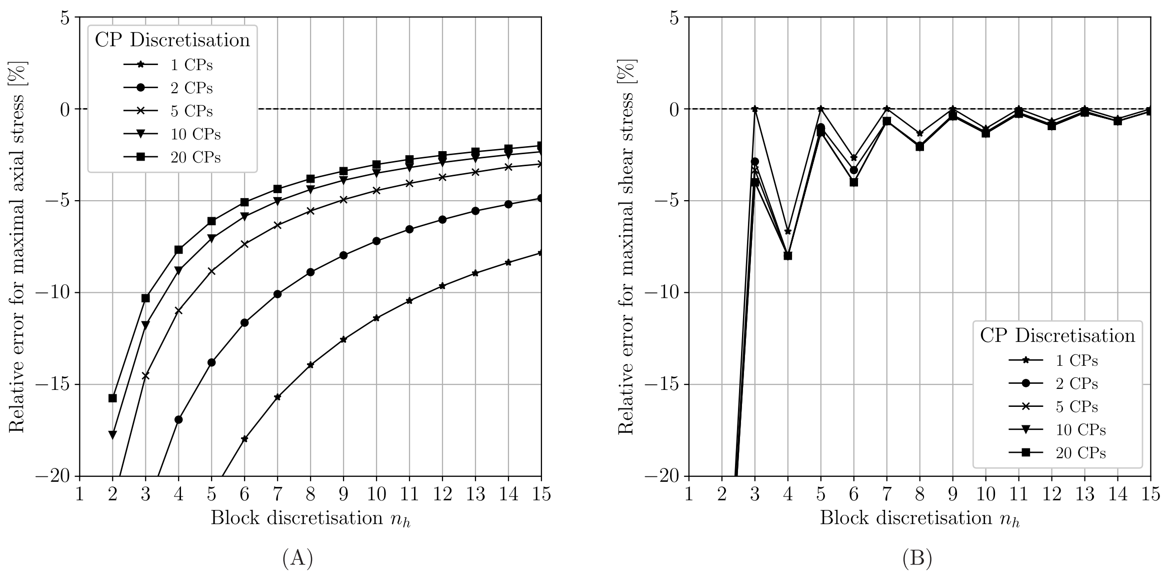

Fig. 15. Convergence study to assess the influence of the block and CP discretizations on the maximal (A) axial and (B) shear stresses.

the maximal axial and shear stresses. In these graphs, the percentage error is evaluated as the difference between computed and analytical maximal stress, divided by the latter. This study shows that HybriDFEM provides a lower-bound estimate of the maximal axial stress, with an error that is decreasing with both block and CP increased refinement. Comparing the error obtained for the beam herein discretized in both directions with the beam presented in [11], it can be concluded that the error depends only on the longitudinal block discretization and on the CP discretization, and not on the transverse block discretization. The smallest error reaches −2% for the finest beam discretization, with $n_h = 15$ and $n_{CP} = 20$.

Regarding the maximal shear stress, the error approaches 0% when the transverse block discretization n_h is performed with an odd number of blocks. This can be explained by the fact that the shear stress is constant along each block and is evaluated with an error close to 0 at the center of each CF, as can be seen in Fig. 13. Since the maximum shear stress is reached at the center of the beam, discretizations with an odd number of blocks are more accurate in its simulation. Another consequence of the fact that the shear stress distribution is constant along each CF, is that the CP discretization only has a slight influence on the precision, unlike what happens for the maximal axial stress. Its effect is visible only for the coarsest CP and block discretizations.

5.2. Plastic frame with cyclic loading

The rigid node connections implemented in HybriDFEM are validated in this second example, together with a first application of the HybriDFEM to cyclic loading. The example consists of a one-storey one-bay 3 m × 3 m frame made of a continuous material. The flexural stiffness of the two columns is twice that of the beam, which has a square cross-section of 0.2 m × 0.2 m. The HybriDFEM model of the frame consists of three beam-like members representing the columns and the beam, each subdivided into 30 blocks in their longitudinal direction and rigidly connected at their extremities. A simple support is placed at the bottom of each column, blocking the translational DoFs of their respective lowest blocks. All the CFs are discretized into 20 CPs each.

The adopted material model is a rate-independent perfectly plastic model in the axial direction, and an elastic model in the shear direction :

$$\begin{cases} \sigma = E_0\left(\varepsilon - \varepsilon_p\right) & \text{when} \quad |\varepsilon - \varepsilon_p| < f_y/E_0 \\ \sigma = f_y & \text{when} \quad |\varepsilon - \varepsilon_p| \geq f_y/E_0 \\ \tau = G_0\gamma, & \end{cases} \tag{19}$$

with $f_y = 20$ MPa, $E_0 = 30$ GPa and $G_0 = 15$ GPa. Through the use of a return-mapping algorithm [93], the material model can handle residual plastic deformations ε_p. This feature will be highlighted by applying a cyclic loading on the frame: a horizontal force F is applied at the top left corner of the frame, and is controlled by means of a displacement-controlled procedure on the horizontal displacement of the node on which the force is applied. During the simulation, a cyclically increasing horizontal displacement is imposed at the top of the frame, as shown in Fig. 16A. This example was already introduced by the authors for a monotonic loading [73].

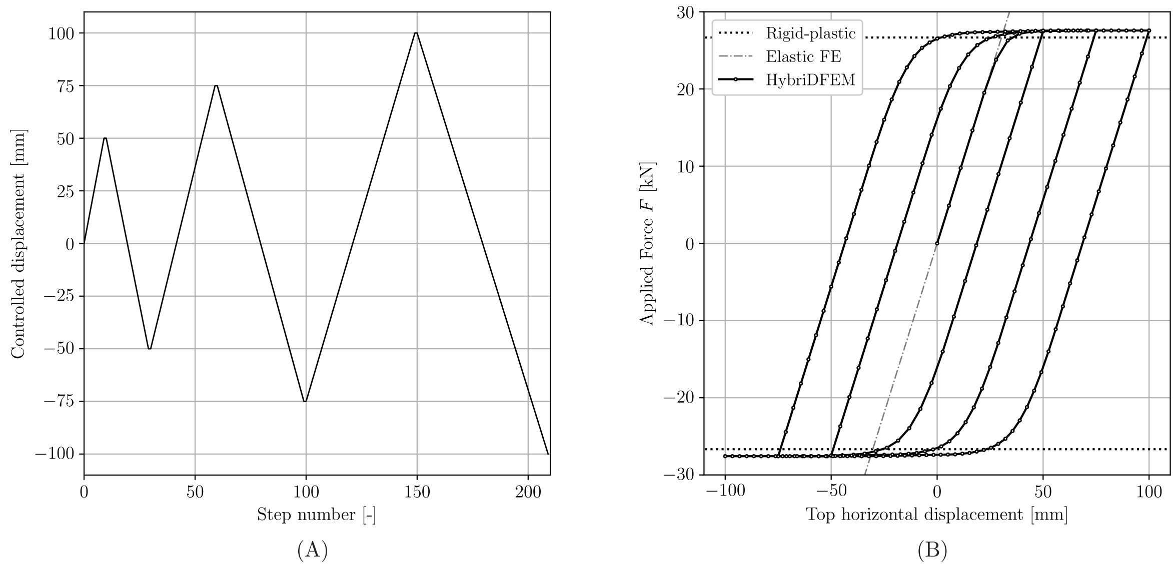

Fig. 16. (A) Displacement path imposed to the plastic frame and (B) its force–displacement response.

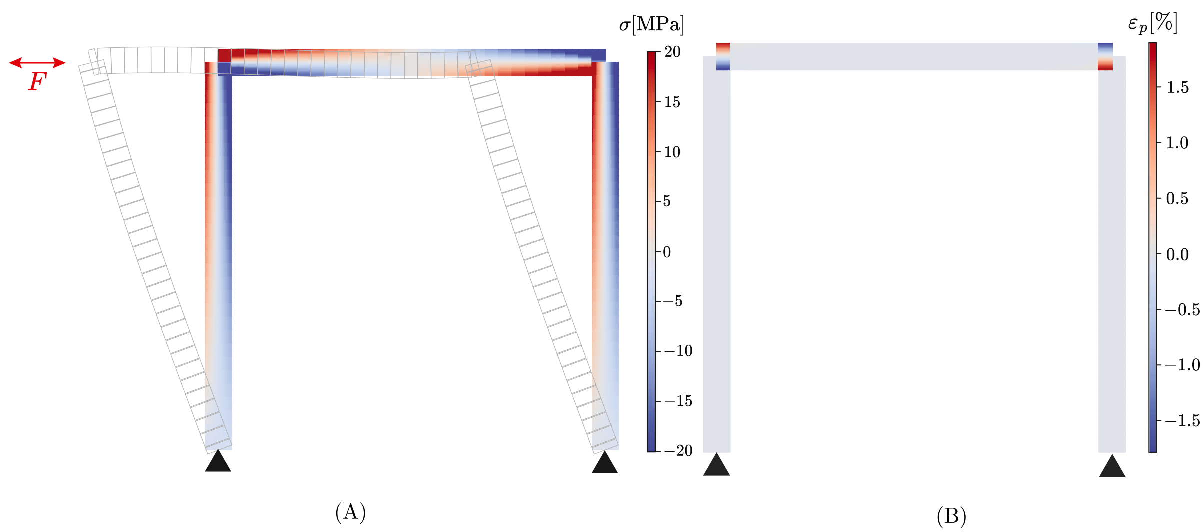

Fig. 17. (A) Axial stresses and deformed shape (×10) and (B) accumulated plastic strains in the HybriDFEM frame at the end of the simulation, at an imposed horizontal displacement of −100 mm.

The results of the HybriDFEM simulation are compared with the analytical solution of the rigid-plastic equivalent frame. Using the beam plastic moment, the maximal resisting force F_{max} = 26.7 kN of the frame can be derived. The yield force F_y = 17.6 kN, at which the first material yielding occurs in the outermost sectional fiber, can also be derived analytically from the beam's elastic moment. Fig. 16B shows that both the yield force and the maximal force of the frame are accurately reproduced by the HybriDFEM model. The slight overestimation of both values with the HybriDFEM model can be explained by the fact that the plastic hinges do not form exactly at the corner of the frame, but rather at the first CF inside the beam, next to the corner nodes.

An equivalent frame made of three linear Timoshenko finite elements [91,94] is used to validate the elastic branch of the HybriDFEM frame response. Fig. 16B shows that the initial slope of the HybriDFEM frame follows closely the response of the linear elastic FE model, up to the yielding point. Once plastic deformations occur in the frame, the force–displacement response of the frame still follows the same slope as for the linear FE model in the unloading phases. This figure shows that the HybriDFEM model is able to capture complex nonlinear material effects that include residual deformations. The axial stresses in the frame are shown in Fig. 17A, along with its deformed shape at the end of the simulation, magnified by a factor 10. The appearance of plastic hinges in the beam at the corners of the frame is visible in Fig. 17B, while the columns remain elastic.

5.3. In-plane capacity of a small masonry wall

As an illustration example for the force–displacement approach, a small masonry wall is modeled with HybriDFEM. The bricks composing the wall have dimensions $h \times b$ = 0.2 m × 0.4 m (or 0.2 m × 0.2 m for the half-bricks) and the wall is composed of three rows of bricks, each three bricks long (or extending over two half-bricks and two full bricks) lying on a three-bricks-long base block fixed in the three directions, as depicted in Fig. 18A.

The contact law used to simulate the interaction between the bricks is a Coulomb friction spring law as described in Section 4.1, with zero cohesion (c = 0) and zero tensile strength (F_y = 0), representing dry-stacked masonry. The initial normal and tangential stiffness are both equal to k_{nn} = k_{ss} = 10^5 kN/m. The friction angle is 33°, which corresponds to a friction coefficient μ = 0.65. Only two CPs are placed

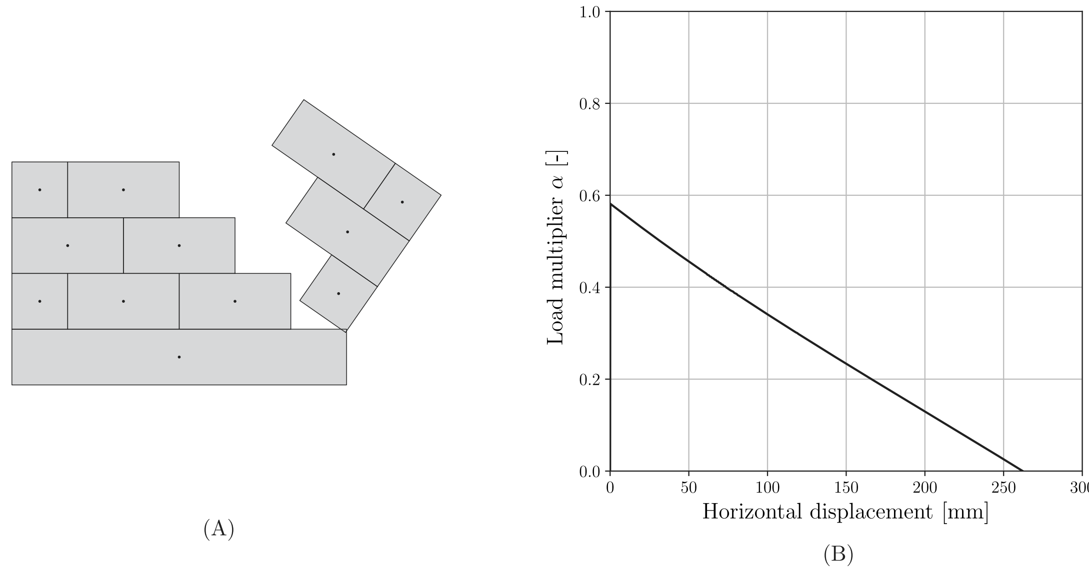

Fig. 18. (A) Collapse mechanism of the small masonry wall at its ultimate displacement $\Delta_{max} = 262$ mm. (B) Pushover curve of the wall.

at each CF, each at a distance of 0.02 m from the edge of the CF. This is equivalent to truncating each corner by 0.02 m, as is often done in DEM simulations to represent concentrated damage at the corners of the bricks [15,56,95].

In addition to the self-weight W (with $\rho = 10$ kN/m^2) of each block, a horizontal load is applied at the center of mass of every block to simulate seismic action. This horizontal load is proportional to the weight of the block by a factor α referred to as the load multiplier. The value of α is controlled by a displacement-controlled procedure on the horizontal displacement of the centroid of the rightmost upper block, referred to as Δ.

Fig. 18A, which represents the deformed shape of the wall at its ultimate displacement $\Delta_{max} = 262$ mm, for which the corresponding α equals 0, shows that the collapse mechanism consists of a wall portion composed of two full bricks and two half bricks, rocking around the bottom right corner of its lowest half brick. More specifically, the wall portion that is forming the mechanism is rocking around the rightmost CP, at 2 cm from the edge of the block.

Fig. 18B shows the pushover curve of the wall, which consists of an ascending branch while the mechanism progressively detaches from the rest of the wall, up to a maximal load multiplier $\alpha_{max} = 0.581$ at a control displacement of 0.175 mm, approximately. At the start of the simulation, the first CPs to be deleted are the ones located on the head joints along the crack. Next, the CPs on the bed joints along the crack are progressively deleted, starting with the ones located on the upper left bed joint. The CP located on the left of the bottom right bed joint, on the same CF as the pivot point, disappears at a control displacement of around 0.175 mm. This is clearly visible when zooming in on the ascending branch (Fig. 19), as the branch is piece-wise linear, with a stiffness drop each time a new CP is deleted. Even if the collapse mechanism is dominated by the wall portion rocking around one CP, small sliding was observed in the bed joints in the ascending branch.

When the simulation reaches the maximal load multiplier (also called collapse load multiplier), the full mechanism has formed, and the detached wall portion starts to rock around its tipping point. Other wall configurations, which included openings, have already been modeled with HybriDFEM to assess their in-plane capacity, but the nonlinear geometric effects were not included and only the maximal load multiplier was computed [72]. Including the effects of large displacements in the simulation allows capturing the descending branch of the curve, which diminishes the collapse load multiplier (c.f. [72]) and pushes the mechanism up to a point where the wall will collapse even without applying any additional horizontal force, corresponding to its ultimate displacement $\Delta_{max} = 262$ mm.

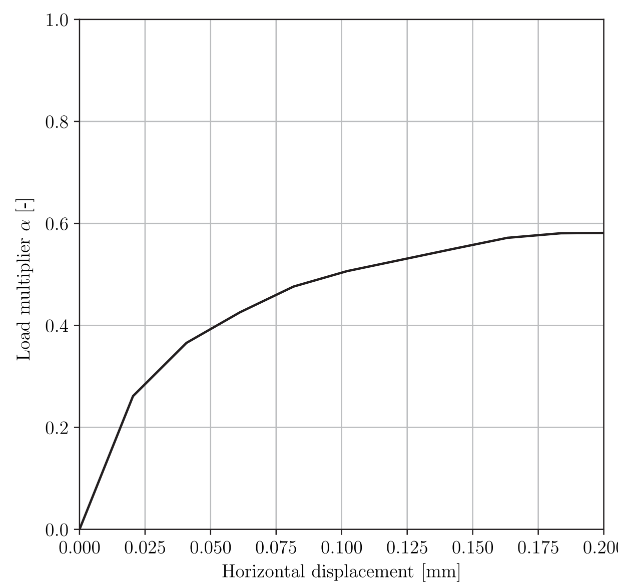

Fig. 19. Ascending branch of the pushover curve of the small masonry wall.

Applying a pattern of forces on a multi-block structure like the small masonry wall presented here is a challenge when using a classical displacement-controlled strategy with DEM formulations that make use of time-stepping algorithms. Strategies to overcome this difficulty in DEM have been presented in [15,96], but none of them is based on the static equilibrium of the system. In [71], a modeling approach based on mathematical programming was proposed as a proxy. The results presented in this example are therefore a new contribution towards full equilibrium-based displacement-controlled strategies to obtain the post-peak behavior of blocky structures.

5.4. Masonry frames under lateral force

In this example, the capability of HybriDFEM to model 2D assemblies of blocks of various size that are not necessarily arranged according to a regular pattern, is evaluated. The original problem is

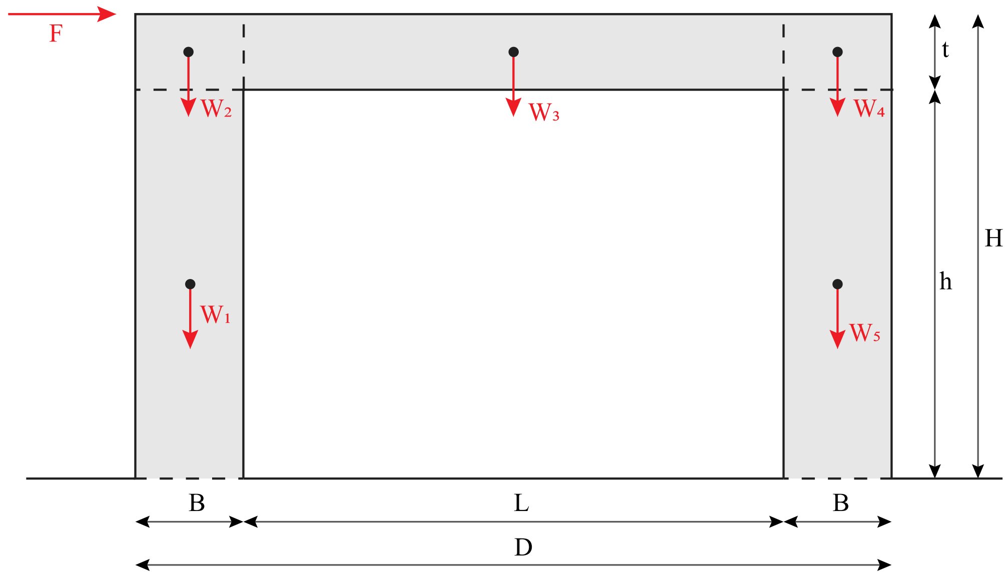

Fig. 20. Geometry of the masonry frame, with potential cracks indicated by dashed lines [73].

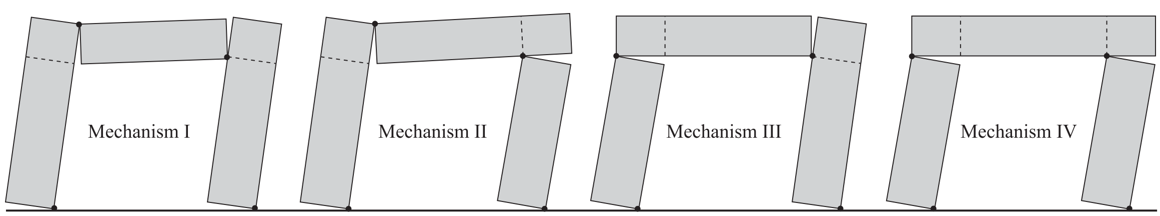

Fig. 21. The four collapse mechanisms analyzed by Giordano et al. [97].

taken from [97], where limit analysis was used to evaluate the collapse load and collapse mechanism of heavy masonry frames.

In the original study [97], analytical expressions were derived to determine the collapse load multiplier α_{max} of a masonry frame subjected to its self weight and a lateral force applied on its top left corner. The collapse load multiplier was defined as the ratio between F_{max}, the force triggering the collapse mechanism, and W_{tot}, the total weight of the frame. The authors of the cited study made the assumption that cracks in the masonry frames could occur only in the pier-to-spandrel connections, which brought them to analyze the frame as an assembly of five blocks (Fig. 20). Between the blocks, zero tensile strength and no possibility of sliding were assumed.

Under this configuration, 15 possible collapse mechanisms can be generated [97]. The one associated with the lowest collapse load multiplier depends on the aspect ratios t/H, B/D and H/D of the frame. Of all the possible mechanisms, some were discarded because the associated displacements were incompatible with the applied horizontal force, others because they were considered unlikely to occur in real structures [97]. The analytical expressions for α_{max} were formulated for the four mechanisms illustrated in Fig. 21.

The frame itself is modeled in HybriDFEM using 5 blocks as in the original discretization (Fig. 20). An extra block, 20% larger than the frame and whose DoFs are blocked, is placed at the base of the frame. An additional $1\ \mathrm{mm} \times 1\ \mathrm{mm}$ block is used to transfer the lateral force to the upper left corner of the frame as in the analytical model. This block is so small that it is not visible in the model (Figs. 22A, 23A).

A force–displacement approach is adopted for modeling contact, with only two CPs for each CF. In order to compare the results of HybriDFEM with the ones of limit analysis, no offset is considered at the corners of the blocks and the CPs are hence placed at their extremities. For all the CPs the following elastic-no tension contact law is adopted:

$$\begin{cases} F_n = k_{nn}\Delta L_n \quad \text{and} \quad F_s = k_{ss}\Delta L_s & \text{when} \quad \Delta L_n \leq 0 \\ F_n = 0 \quad \text{and} \quad F_s = 0 & \text{when} \quad \Delta L_n > 0, \end{cases} \tag{20}$$

with a high contact stiffness being assigned in order to approach a rigid-no tension behavior $k_{nn} = 10^{10}$ kN/m. To limit the sliding between the blocks it is chosen to assign an even higher tangential stiffness $k_{ss} = 100 \times k_{nn}$.

A first implementation of this example via HybriDFEM was presented in [73]. The results presented here are an extension of said study in that:

- The CPs are placed at the extremities of the CFs instead of distributing them uniformly. This allows, on one hand, reducing the computational time, and, on the other, modeling potential cracks with sharp corners, as done in the original study [97].
- Instead of the force-controlled procedure previously adopted, a displacement-controlled procedure is here applied, controlling the horizontal displacement of the loading block. This allows capturing the post-peak behavior of the masonry frame.
- The lateral force is applied directly at the top left corner of the frame via the loading block. Previously, the force was applied on the centroid of the top left block, with an additional moment $M = Ft/2$ accounting for the eccentricity. In some cases, this led to predicting different mechanisms.

The capacity of HybriDFEM to predict the correct collapse load multiplier and collapse mechanism was already demonstrated for twelve different geometries in [73]. Therefore, here the focus is placed on

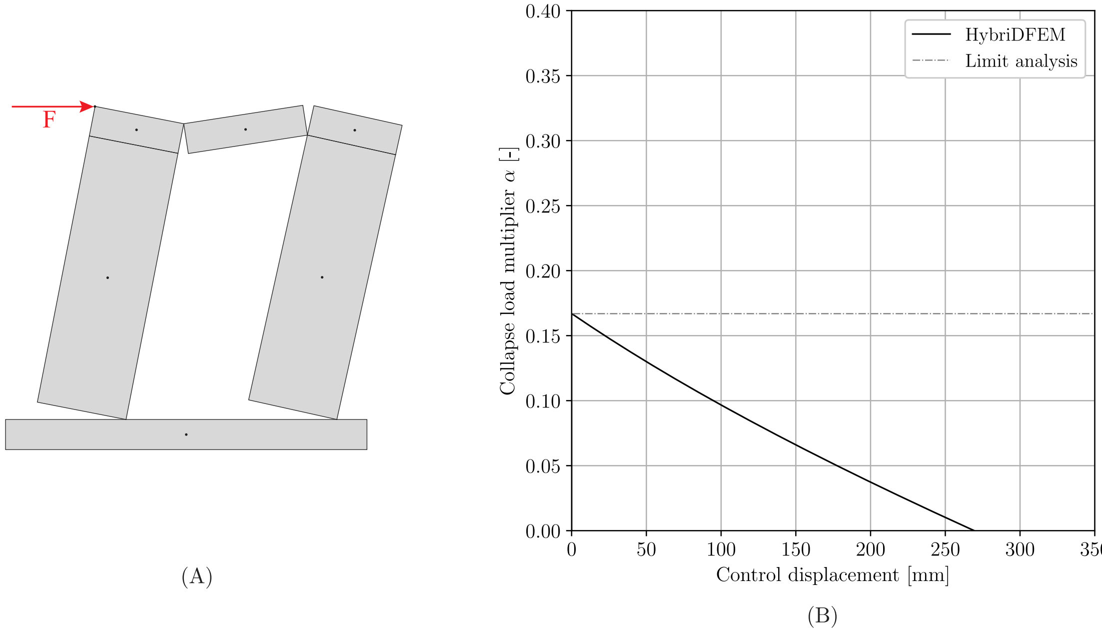

Fig. 22. (A) Collapse mechanism of the masonry frame with $B/D = 0.3$ and $t/H = 0.1$ at a control displacement of 200 mm, and (B) pushover curve.

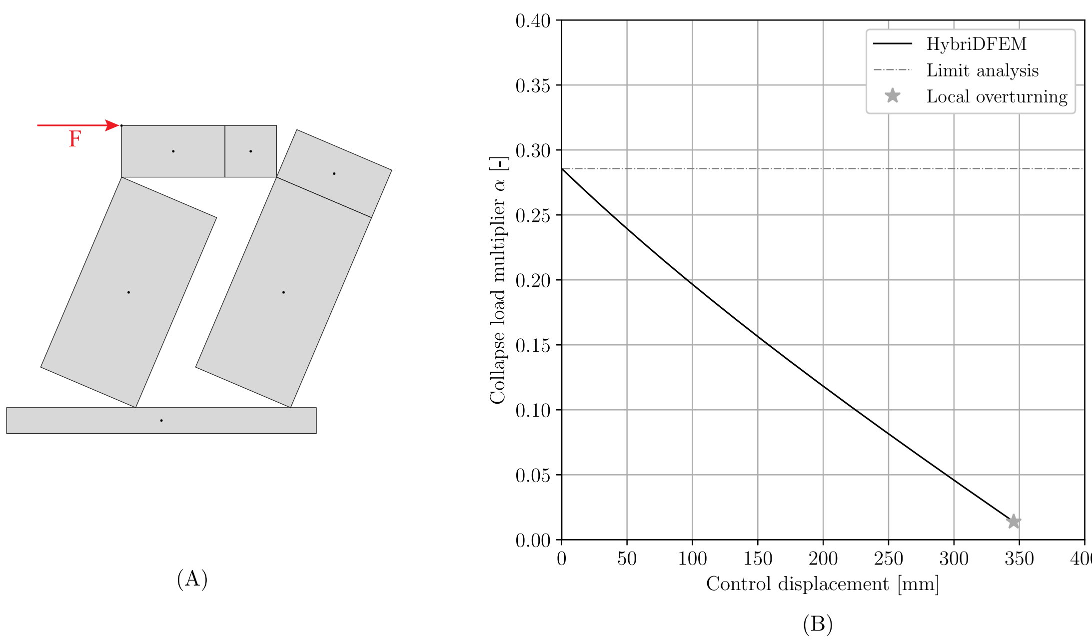

Fig. 23. (A) Collapse mechanism of the masonry frame with $B/D = 0.4$ and $t/H = 0.2$ at a control displacement of 200 mm, and (B) pushover curve.

two specific frame geometries, including the analysis of their post-peak behavior. For both frames, a ratio $H/D = 1$, with $H = 1$ m, is adopted. Depending on the values adopted for t/H and B/D, the collapse mechanism differs. For the first frame, with $t/H = 0.1$ and $B/D = 0.3$, limit analysis predicts mechanism I with $\alpha_{max} = 0.167$, whereas for the second frame, with $t/H = 0.2$ and $B/D = 0.4$, mechanism III is predicted with $\alpha_{max} = 0.286$.

Figs. 22 and 23 show the collapse mechanisms obtained for the two frame geometries at a control displacement of 200 mm, along with the resulting pushover curve. The collapse load multiplier is taken as the maximal value of the pushover curve. For both cases, the collapse load multiplier predicted by limit analysis and the one predicted by HybriDFEM are nearly identical, with the relative error not exceeding 0.05%. Moreover, the mechanisms triggered in HybriDFEM correspond to the ones predicted by limit analysis. Finally, both pushover curves show that the nonlinear geometric effects are captured, displaying a progressive decrease of the capacity of the frame as the control displacement increases, due to $P-\Delta$ effects. For the first frame, an ultimate displacement of 269.3 mm is reached. For the second frame, the ultimate displacement is attained at a non-zero load multiplier: this is associated to the local overturning of the right pier as it completely separated from the rest of the frame.

5.5. Coupling with classical FE: flexible masonry frame

One of the main purposes behind the original development of the HybriDFEM is the intention to couple it with classical finite elements (FEs). This last example illustrates this feature.

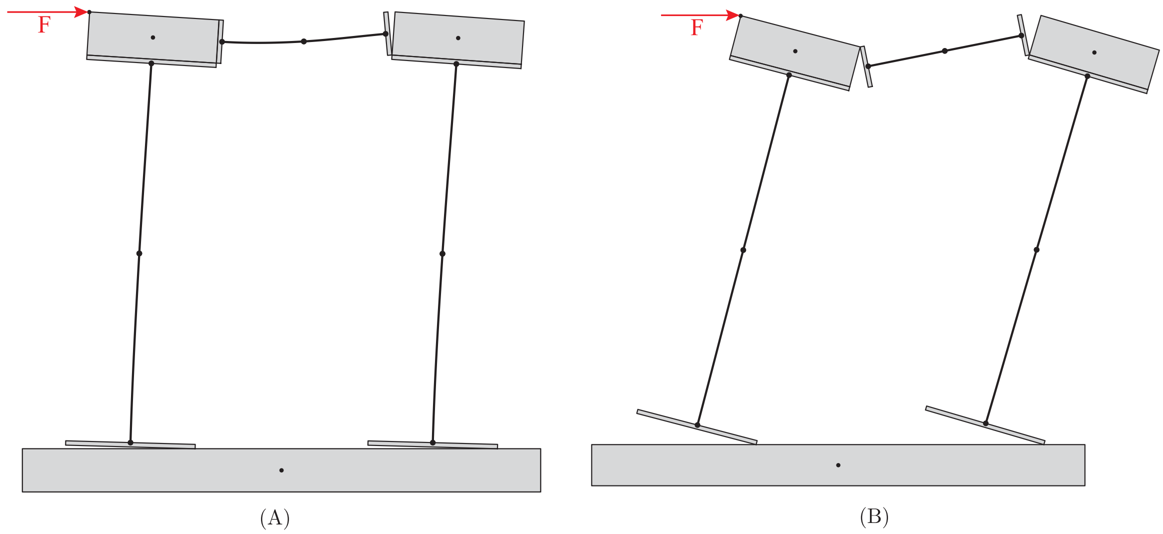

Fig. 24. (A) Deformed shape of the HybriDFEM - FEM frame at the maximal applied load, magnified by a factor 250. (B) Collapse mechanism of the HybriDFEM - FEM frame at a control displacement of 200 mm.

The masonry frame presented in Section 5.4 with $t/H = 0.1$ and $B/D = 0.3$ is reconsidered. The assumption that the cracks can only occur at pier-to-spandrel connections is upheld, with the addition that the piers and spandrel do not behave as rigid blocks anymore, but can rather deform elastically. Therefore, the blocks representing the piers and spandrels are each replaced by two Timoshenko FEs accounting for the effect of large displacements [91,94]. The total weight of the block is applied at the connection between the two FEs representing the block, which corresponds to its center of mass. At the other end of each FE, a 1 cm-thick HybriDFEM block is attached such that the potential crack at the connection with the corner or base block is modeled as a CF (Fig. 24A). As in the previous examples, the CFs are composed of two CPs placed at their edges, with the same force–displacement law assigned to the springs. For all the blocks, the same dimensions as the previously presented frame are used and a Young's modulus $E = 5$ GPa and Poisson's ratio $\nu = 0.0$ are assumed for all the FEs. The blocks representing the pier-to-spandrel connections, the support block and the loading block are modeled as rigid blocks, as previously. The displacement-controlled procedure applied to the frame is also identical to the one described in Section 5.4.

The obtained collapse mechanism and pushover curve are depicted in Figs. 24 and 25. Both for the flexible model and the rigid one, the maximal load multiplier is 0.167 and the ultimate displacement is 269.3 mm. The response of the frame in the descending branch of the pushover is still dominated by rocking, and mechanism I is obtained, as was the case for the rigid frame. However, the effect of the flexibility is visible when looking at the slope of the ascending branch, where the response is dominated by the deformation of the flexible piers. Indeed, the control displacement when the collapse load is reached is 0.1 mm, whereas for the rigid case the collapse load was attained for an imposed displacement of 3×10^{-5} mm. Fig. 24A shows the deformed shape of the flexible frame, magnified by a factor 250, when the maximal load multiplier is reached.

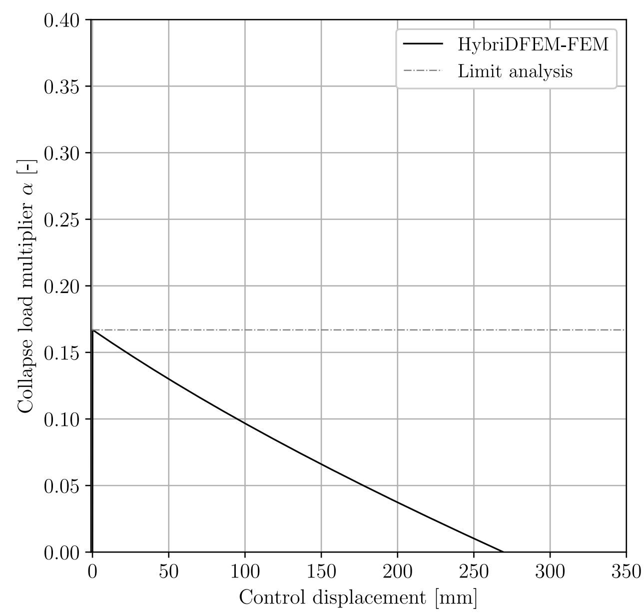

Fig. 25. Pushover curve of the HybriDFEM - FEM frame.

6. Discussion

The extensions to the HybriDFEM method shown in Fig. 1 were validated using numerical examples ranging from linear elastic beams to dry-stacked masonry walls, highlighting the diverse range of applications of the method:

- In Section 2, the procedure presented in [11] for evaluating the resisting forces of a 1D structure with HybriDFEM has been extended to accommodate 2D geometries. These consist of assemblies of quadrilateral blocks of various geometries, not aligned with each other, and with the possibility of being in contact with other blocks on all sides. This procedure has proven valid in several examples presented in Section 5. For instance, the axial and shear stress distribution in a linear elastic beam was evaluated in Section 5.1, highlighting the capability of HybriDFEM to capture Saint-Venant's effect.
- Also in Section 2, rigid node connections were presented, allowing assemblies of unaligned 1D-members such as frames to be modeled. This feature also allows the coupling of HybriDFEM elements with classical FEs. These rigid node connections have been used in several examples, notably in Section 5.5 for modeling a masonry frame composed of discrete blocks, where coupling with FEs accounted for the deformability of the masonry piers.
- The application of cyclic loading was implemented along with the introduction of contact models that include residual deformations. This feature was highlighted in Section 5.2, in an example

consisting of a continuous frame, which was composed of an elastic-perfectly plastic material subjected to cyclic loading. This also enabled the consideration of sliding in the evaluation of the in-plane capacity of a small masonry wall.

- In Section 3, an automatized procedure to detect edge-to-edge contacts in a given block discretization was presented. The procedure is applied at the start of the simulation and can handle contact deletion and recovery throughout the simulation. This algorithm has been successfully applied in all examples presented in Section 5, some of which involve blocks in contact only through parts of their edges or completely surrounded by other blocks. Improvements to enhance the algorithm's efficiency will be explored in future work.
- Allowing the user to choose where to locate the contact pairs (CPs) along the contact faces (CFs) is a new feature enabling the simulation, for example, of masonry blocks with sharp or rounded corners. In this manner, the pushover curves of a masonry wall with rounded corners and a masonry frame with sharp corners were evaluated using only two CPs per CF (Sections 5.3–5.5). The minimization of the number of CPs considerably reduces computation time.
- Depending on the problem at hand, the user can now choose between three different approaches for modeling contact: a force–displacement approach, which is best suited when modeling a structure exhibiting vertex-to-edge contacts or, in the future, to model reinforcing rebars in composite structures; a stress–strain approach, where the material properties of the blocks are scaled and assigned to the associated bidirectional springs to represent the behavior of a continuous structure; or a stress–displacement approach, which proves useful for modeling the behavior of flexible zero-thickness interfaces. These various approaches have been tested and validated in the different examples presented in Section 5.

7. Conclusions

In this paper, it was shown how the HybriDFEM method, a discrete formulation, can be used in a hybrid model incorporating classical finite elements. This significant advantage enables optimal use of both modeling approaches within a single framework, to improve overall computational efficiency. It has now been shown how HybriDFEM can be used to model frames and biaxially-discretized (2D) structures, thus significantly expanding the scope of the method, which was previously limited to uniaxially-discretized (1D) structures such as columns and beams. A two-step algorithm for detecting contact interfaces has been described. The algorithm first identifies pairs of blocks potentially in contact through an initial assessment using the smallest enclosing circle, followed by the narrow detection of contact among the identified pairs. This algorithm has the advantage of being relatively simple to implement while remaining efficient due to its two-step contact detection process. Finally, three distinct approaches for modeling contact were presented. They allow HybriDFEM to effectively model structures and systems of blocks as diverse as continuous frames, flexible mortar interfaces, and blocks rocking on top of one another.

Ongoing developments of the method include the extension to dynamic analyses, using both modal superposition and nonlinear time-stepping algorithms to simulate the response of a structure under more extreme dynamic loadings, potentially up to full collapse. Another promising extension of the method is its application to reinforced concrete structures. One of the most attractive features of HybriDFEM, namely the possibility to couple it with classical FEs, will also be further investigated, by using more advanced FEM formulations (e.g., themselves accounting for material nonlinearities) and nonlinear node connections instead of rigid ones, to model, e.g., detachment of an FE from a HybriDFEM block. These HybriDFEM-FEM coupled models will offer the possibility to explicitly model discrete systems while taking advantage of the computational efficiency of the finite elements in zones of the structure where the behavior is more akin to that of a continuum.

CRediT authorship contribution statement

Igor Bouckaert: Writing – review & editing, Writing – original draft, Visualization, Validation, Software, Methodology, Investigation, Formal analysis, Conceptualization. **Michele Godio:** Writing – review & editing, Writing – original draft, Supervision, Methodology, Conceptualization. **João Pacheco de Almeida:** Writing – review & editing, Writing – original draft, Supervision, Resources, Methodology, Funding acquisition, Conceptualization.

Declaration of competing interest

The authors declare that they have no known competing financial interests or personal relationships that could have appeared to influence the work reported in this paper.

Acknowledgments

The first author is thankful for the financial support given by UCLouvain, Belgium. The support of Prof. Alberto Taliercio (Politecnico di Milano) and Prof. Rui Pinho (University of Pavia) as part of the first author's supervisory panel is also greatly acknowledged.

References

[1] Ferrante A, Giordano E, Clementi F, Milani G, Formisano A. FE vs. DE modeling for the nonlinear dynamics of a historic church in central Italy. Geosciences 2021;11(5). http://dx.doi.org/10.3390/geosciences11050189.

[2] Malomo D, Pulatsu B. Discontinuum models for the structural and seismic assessment of unreinforced masonry structures: a critical appraisal. Structures 2024;62. http://dx.doi.org/10.1016/j.istruc.2024.106108.

[3] Zhou X, Feng B. A smeared-crack-based field-enriched finite element method for simulating cracking in quasi-brittle materials. Theor Appl Fract Mech 2023;124:103817. http://dx.doi.org/10.1016/j.tafmec.2023.103817, URL: https://www.sciencedirect.com/science/article/pii/S0167844223000691.

[4] Krejčí T, Koudelka T, Bernardo V, Šejnoha M. Effective elastic and fracture properties of regular and irregular masonry from nonlinear homogenization. Comput Struct 2021;254:106580. http://dx.doi.org/10.1016/j.compstruc.2021.106580, URL: https://www.sciencedirect.com/science/article/pii/S0045794921001024.

[5] Fattahi M, Malekshahi M, Permanoon A. Mesoscale numerical modeling of unreinforced masonry wall response to underground dynamic loads: A comparative study utilizing FEM and DEM. Structures 2024;63:106460. http://dx.doi.org/10.1016/j.istruc.2024.106460, URL: https://www.sciencedirect.com/science/article/pii/S235201242400612X.

[6] Chen Z, Zhou Y, Kinoshita T, DeJong MJ. Distinct element modeling of the in-plane and out-of-plane response of ordinary and innovative masonry infill walls. Structures 2023;50:1447–60. http://dx.doi.org/10.1016/j.istruc.2023.02.035, URL: https://www.sciencedirect.com/science/article/pii/S2352012423001935.

[7] Yue Y, Smith B, Chen PY, Chantharayukhonthorn M, Kamrin K, Grinspun E. Hybrid grains: Adaptive Coupling of discrete and continuum simulations of granular media. ACM Trans Graph 2018;37(6):1–19. http://dx.doi.org/10.1145/3272127.3275095, ISSN: 0730-0301 1557-7368.

[8] Bauman PT, Dhia HB, Elkhodja N, Oden JT, Prudhomme S. On the application of the Arlequin method to the coupling of particle and continuum models. Comput Mech 2008;42(4):511–30. http://dx.doi.org/10.1007/s00466-008-0291-1, ISSN: 0178-7675 1432-0924.

[9] Hammoud M, Duhamel D, Sab K. Static and dynamic studies for coupling discrete and continuum media; Application to a simple railway track model. Int J Solids Struct 2010;47(2):276–90. http://dx.doi.org/10.1016/j.ijsolstr.2009.09.036.

[10] Mhada K, Bourihane O. A multi-scale model for global buckling and local wrinkling interaction with application to sandwich beams. Structures 2021;32:1398–407. http://dx.doi.org/10.1016/j.istruc.2021.03.042, URL: https://www.sciencedirect.com/science/article/pii/S2352012421002228.

[11] Bouckaert I, Godio M, Pacheco de Almeida J. A Hybrid Discrete-Finite Element method for continuous and discontinuous beam-like members including nonlinear geometric and material effects. Int J Solids Struct 2024;294. http://dx.doi.org/10.1016/j.ijsolstr.2024.112770.

[12] Cundall PA, Strack ODL. A discrete numerical model for granular assemblies. Géotechnique 1979;29(1):47–65. http://dx.doi.org/10.1680/geot.1979.29.1.47.
[13] Lemos JV. Contact representation in rigid block models of masonry. Int J Mason Res Innov 2017;2(4):321. http://dx.doi.org/10.1504/ijmri.2017.087445.
[14] Pulatsu B, Erdogmus E, Lourenço PB, Lemos JV, Tuncay K. Simulation of the in-plane structural behavior of unreinforced masonry walls and buildings using DEM. Structures 2020;27:2274–87. http://dx.doi.org/10.1016/j.istruc.2020.08.026, URL: https://www.sciencedirect.com/science/article/pii/S2352012420304173.
[15] Bouckaert I, Godio M, Pacheco de Almeida J. A strategy for generating pushover curves of block assemblies including post-peak branch using the discrete element method. In: COMPDYN 2022. 2022.
[16] Bertolesi E, Milani G, Casolo S. Homogenization towards a mechanistic Rigid Body and Spring Model (HRBSM) for the non-linear dynamic analysis of 3D masonry structures. Meccanica 2017;53(7):1819–55. http://dx.doi.org/10.1007/s11012-017-0665-6, ISSN: 0025-6455 1572-9648.
[17] Casolo S. Macroscale modelling of microstructure damage evolution by a rigid body and spring model. J Mech Mater Struct 2009;4:551–70. http://dx.doi.org/10.2140/jomms.2009.4.551.
[18] Portioli F, Cascini L. Large displacement analysis of dry-jointed masonry structures subjected to settlements using rigid block modelling. Eng Struct 2017;148:485–96. http://dx.doi.org/10.1016/j.engstruct.2017.06.073.
[19] Portioli FPA, Lourenço PB. Nonlinear static analysis of masonry structures with mortar joints and cracking units by optimization-based rigid block models. Earthq Eng Struct Dyn 2024;53(13):3963–82. http://dx.doi.org/10.1002/eqe.4206, URL: https://onlinelibrary.wiley.com/doi/abs/10.1002/eqe.4206, arXiv:https://onlinelibrary.wiley.com/doi/pdf/10.1002/eqe.4206.
[20] Meguro K, Tagel-din H. Applied element method for structural analysis: Theory and application for linear materials. Struct Eng/Earthq Eng, JSCE 2000;17.
[21] Meguro K, Tagel-Din H. Applied element method used for large displacement structural analysis. J Natur Disaster Sci 2002;24:25–34.
[22] Malomo D, Scattarreggia N, Orgnoni A, Pinho R, Moratti M, Calvi GM. Numerical study on the collapse of the morandi bridge. J Perform Constr Facil 2020;34(4):04020044. http://dx.doi.org/10.1061/(ASCE)CF.1943-5509.0001428.
[23] da Silva LC, Milani G, Lourenço PB. Probabilistic-based discrete model for the seismic fragility assessment of masonry structures. Structures 2023;52:506–23. http://dx.doi.org/10.1016/j.istruc.2023.04.015, URL: https://www.sciencedirect.com/science/article/pii/S2352012423004885.
[24] Ke L, Van Der Meer F. A computational homogenization framework with enhanced localization criterion for macroscopic cohesive failure in heterogeneous materials. J Theor Comput Appl Mech 2022.
[25] Drougkas A, Sarhosis V, D'Alessandro A, Ubertini F. Homogenisation of masonry structures subjected to seismic loads through matrix/inclusion micromechanics. Structures 2022;38:375–84. http://dx.doi.org/10.1016/j.istruc.2022.02.016, URL: https://www.sciencedirect.com/science/article/pii/S2352012422001072.
[26] Barros JA, Baghi H, Ventura-Gouveia A. Assessing the applicability of a smeared crack approach for simulating the behaviour of concrete beams flexurally reinforced with GFRP bars and failing in shear. Eng Struct 2021;227:111391. http://dx.doi.org/10.1016/j.engstruct.2020.111391, URL: https://www.sciencedirect.com/science/article/pii/S0141029620339924.
[27] Lourenço PB, Milani G, Tralli A, Zucchini A. Analysis of masonry structures: review of and recent trends in homogenization techniquesthis article is one of a selection of papers published in this special issue on masonry. Can J Civil Eng 2007;34(11):1443–57. http://dx.doi.org/10.1139/L07-097, arXiv:https://doi.org/10.1139/L07-097.
[28] Cluni F, Gusella V. Homogenization of non-periodic masonry structures. Int J Solids Struct 2004;41(7):1911–23. http://dx.doi.org/10.1016/j.ijsolstr.2003.11.011, URL: https://www.sciencedirect.com/science/article/pii/S0020768303006474.
[29] Meftah SA, Aldosari SM, Tounsi A, Cuong-Le T, Khedher KM, Alluqmani AE. Simplified homogenization technique for nonlinear finite element analysis of in-plane loaded masonry walls. Eng Struct 2024;306:117822. http://dx.doi.org/10.1016/j.engstruct.2024.117822, URL: https://www.sciencedirect.com/science/article/pii/S0141029624003845.
[30] Sanahuja J, Toulemonde C. Numerical homogenization of concrete microstructures without explicit meshes. Cem Concr Res 2011;41(12):1320–9. http://dx.doi.org/10.1016/j.cemconres.2011.03.023, URL: https://www.sciencedirect.com/science/article/pii/S0008884611000998. Conferences Special: Cement Hydration Kinetics and Modeling, Quebec City, 2009 & CONMOD10, Lausanne, 2010.
[31] Gal E, Kryvoruk R. Properties of concrete: A two step homogenization approach. Comput Model Concr Struct 2010;137.
[32] Denisiewicz A, Kuczma Ma, Kula K, Socha T. Influence of boundary conditions on numerical homogenization of high performance concrete. Materials 2021;14(4). http://dx.doi.org/10.3390/ma14041009, URL: https://www.mdpi.com/1996-1944/14/4/1009.
[33] Alforno M, Monaco A, Venuti F, Calderini C. Validation of simplified micro-models for the static analysis of masonry arches and vaults. Int J Archit Herit 2021;15(8):1196–212. http://dx.doi.org/10.1080/15583058.2020.1808911.
[34] Ma Z, Shi CZ, Wu HG. Numerical cracking analysis of steel-lined reinforced concrete penstock based on cohesive crack model. Structures 2021;34:4694–703. http://dx.doi.org/10.1016/j.istruc.2021.10.048, URL: https://www.sciencedirect.com/science/article/pii/S2352012421010055.
[35] Zhang Y, Huang J, Yuan Y, Mang HA. Cracking elements method with a dissipation-based arc-length approach. Finite Elem Anal Des 2021;195:103573. http://dx.doi.org/10.1016/j.finel.2021.103573, URL: https://www.sciencedirect.com/science/article/pii/S0168874X21000573.
[36] Ooi E, Yang Z. A hybrid finite element-scaled boundary finite element method for crack propagation modelling. Comput Methods Appl Mech Engrg 2010;199(17):1178–92. http://dx.doi.org/10.1016/j.cma.2009.12.005, URL: https://www.sciencedirect.com/science/article/pii/S0045782509004113.
[37] Wawrzynek PA, Ingraffea A. Interactive finite element analysis of fracture processes: an integrated approach. Theor Appl Fract Mech 1987;8(2):137–50.
[38] Rots JG, Nauta P, Kuster G, Blaauwendraad J. Smeared crack approach and fracture localization in concrete. HERON 1985;30(1).
[39] Daux C, Moës N, Dolbow J, Sukumar N, Belytschko T. Arbitrary branched and intersecting cracks with the extended finite element method. Internat J Numer Methods Engrg 2000;48(12):1741–60. http://dx.doi.org/10.1002/1097-0207(20000830)48:12<1741::AID-NME956>3.0.CO;2-L, Cited by: 917; All Open Access, Green Open Access.
[40] Wei P, Wang MY, Xing X. A study on X-FEM in continuum structural optimization using a level set model. Comput Aided Des 2010;42(8):708–19. http://dx.doi.org/10.1016/j.cad.2009.12.001, URL: https://www.sciencedirect.com/science/article/pii/S0010448509003066. Application-driven Shape Development.
[41] Giamundo V, Sarhosis V, Lignola G, Sheng Y, Manfredi G. Evaluation of different computational modelling strategies for the analysis of low strength masonry structures. Eng Struct 2014;73:160–9. http://dx.doi.org/10.1016/j.engstruct.2014.05.007, URL: https://www.sciencedirect.com/science/article/pii/S0141029614002855.
[42] Abdulla KF, Cunningham LS, Gillie M. Simulating masonry wall behaviour using a simplified micro-model approach. Eng Struct 2017;151:349–65. http://dx.doi.org/10.1016/j.engstruct.2017.08.021, URL: https://www.sciencedirect.com/science/article/pii/S0141029616314833.
[43] López CN, Rojas F, Massone LM. Membrane fiber element for reinforced concrete walls – the benefits of macro and micro modeling approaches. Eng Struct 2022;254:113819. http://dx.doi.org/10.1016/j.engstruct.2021.113819, URL: https://www.sciencedirect.com/science/article/pii/S0141029621018897.
[44] César Chácara NM, Lourenço PB. Simulation of shake table tests on out-of-plane masonry buildings. Part (IV): Macro and micro FEM based approaches. Int J Archit Herit 2017;11(1):103–16. http://dx.doi.org/10.1080/15583058.2016.1238972, arXiv:https://doi.org/10.1080/15583058.2016.1238972.
[45] Baraldi D, Reccia E, Cecchi A. In plane loaded masonry walls: DEM and FEM/DEM models. a critical review. Meccanica 2018;53(7):1613–28. http://dx.doi.org/10.1007/s11012-017-0704-3.
[46] Potapov S, Masurel A, Marin P, Daudeville L. Mixed DEM/FEM modeling of advanced damage in reinforced concrete structures. J Eng Mech 2017;143(2):04016110. http://dx.doi.org/10.1061/(ASCE)EM.1943-7889.0001173.
[47] Sacco E, Addessi D, Sab K. New trends in mechanics of masonry. Meccanica 2018;53(7):1565–9. http://dx.doi.org/10.1007/s11012-018-0839-x.
[48] Malomo D, DeJong MJ. A macro-distinct element model (m-DEM) for simulating the in-plane cyclic behavior of URM structures. Eng Struct 2021;227:111428. http://dx.doi.org/10.1016/j.engstruct.2020.111428, URL: https://www.sciencedirect.com/science/article/pii/S0141029620340293.
[49] Liu L, Ji S. A new contact detection method for arbitrary dilated polyhedra with potential function in discrete element method. Internat J Numer Methods Engrg 2020;121(24):5742–65. http://dx.doi.org/10.1002/nme.6522.
[50] Simulia. Abaqus analysis user's guide, Version 6.14. Dassault Systèmes; 2017.
[51] Wriggers P. Computational contact mechanics. Engineering online learning, Berlin, Heidelberg: Springer; 2006, http://dx.doi.org/10.1007/3-540-32609-9.
[52] Laursen TA, Simo JC. A continuum-based finite element formulation for the implicit solution of multibody, large deformation-frictional contact problems. Internat J Numer Methods Engrg 1993;36(20):3451–85. http://dx.doi.org/10.1002/nme.1620362005.
[53] Munjiza A, Rougier E, John NWM. MR linear contact detection algorithm. Internat J Numer Methods Engrg 2006;66(1):46–71. http://dx.doi.org/10.1002/nme.1538.
[54] Itasca. UDEC 7.0. Minneapolis, USA; 2022, URL: https://www.itascacg.com/software/udec/.
[55] Israelsson JI. Short Descriptions of UDEC and 3DEC. Dev Geotech Eng 1996;79:523–8. http://dx.doi.org/10.1016/S0165-1250(96)80041-1.
[56] Lemos JV. The basis for masonry analysis with UDEC and 3DEC. In: Computational modeling of masonry structures using the discrete element method. Hershey, PA, USA: IGI Global; 2016, p. 61–89. http://dx.doi.org/10.4018/978-1-5225-0231-9.ch003.

[57] UMontpellier. LMGC90 user version. Montpellier, France; 2023, URL: https://git-xen.lmgc.univ-montp2.fr/lmgc90/lmgc90_user.

[58] Jean M. The non-smooth contact dynamics method. Comput Methods Appl Mech Engrg 1999;177(3):235–57. http://dx.doi.org/10.1016/S0045-7825(98)00383-1, URL: https://www.sciencedirect.com/science/article/pii/S0045782598003831.

[59] Dubois F, Jean M, Renouf M, Mozul R, Martin A, Bagneris M. LMGC90. In: 10e colloque national en calcul des structures. 2011, p. Clé–USB.

[60] Ge H, Quezada JC, Houerou VL, Chazallon C. Three-dimensional simulation of asphalt mixture incorporating aggregate size and morphology distribution based on contact dynamics method. Constr Build Mater 2021;302:124124. http://dx.doi.org/10.1016/j.conbuildmat.2021.124124.

[61] Munjiza A, Andrews KRF. NBS contact detection algorithm for bodies of similar size. Internat J Numer Methods Engrg 1998;43(1):131–49. http://dx.doi.org/10.1002/(SICI)1097-0207(19980915)43:1<131::AID-NME447>3.0.CO;2-S.

[62] Yu P, Zhang Y, Peng X, Chen G, Zhao JX. Distributed-spring edge-to-edge contact model for two-dimensional discontinuous deformation analysis. Rock Mech Rock Eng 2020;53(1):365–82. http://dx.doi.org/10.1007/s00603-019-01917-2.

[63] Lemos JV. Discrete element modeling of the seismic behavior of masonry construction. Buildings 2019;9(2):43.

[64] Ghaboussi J, Barbosa R. Three-dimensional discrete element method for granular materials. Int J Numer Anal Methods Geomech 1990;14(7):451–72. http://dx.doi.org/10.1002/nag.1610140702.

[65] Casapulla C, Maione A. Modelling the dry-contact interface of rigid blocks under torsion and combined loadings: Concavity vs. convexity formulation. Int J Non-Linear Mech 2018;99:86–96. http://dx.doi.org/10.1016/j.ijnonlinmec.2017.11.002.

[66] Orduña A, Lourenço PB. Three-dimensional limit analysis of rigid blocks assemblages. Part I: Torsion failure on frictional interfaces and limit analysis formulation. Int J Solids Struct 2005;42(18):5140–60. http://dx.doi.org/10.1016/j.ijsolstr.2005.02.010.

[67] Meguro K, Tagel-Din H. A new simplified and efficient technique for fracture behavior analysis of concrete structures. In: Proceedings of the third international conference on fracture mechanics of concrete and concrete structures. 2, 1998, p. 911–20.

[68] Kazerani T, Zhao J. Micromechanical parameters in bonded particle method for modelling of brittle material failure. Int J Numer Anal Methods Geomech 2010;34(18):1877–95. http://dx.doi.org/10.1002/nag.884.

[69] Gao F, Stead D, Elmo D. Numerical simulation of microstructure of brittle rock using a grain-breakable distinct element grain-based model. Comput Geotech 2016;78:203–17. http://dx.doi.org/10.1016/j.compgeo.2016.05.019.

[70] Taforel P. Apport de la Méthode des Eléments Discrets à la Modélisation des Maçonneries en Contexte Sismique : Vers une Nouvelle Approche Numérique de la Vulnérabilité Sismique [Ph.D. thesis], 2012.

[71] Portioli FPA, Godio M, Calderini C, Lourenço PB. A variational rigid-block modeling approach to nonlinear elastic and kinematic analysis of failure mechanisms in historic masonry structures subjected to lateral loads. Earthq Eng Struct Dyn 2021;50(12):3332–54. http://dx.doi.org/10.1002/eqe.3512, ISSN: 0098-8847 1096-9845.

[72] Bouckaert I, Godio M, Pacheco de Almeida J. Assessment of the in-plane capacity of masonry walls with the Hybrid Discrete-Finite Element Method. In: 18th world conference on earthquake engineering. 2024.

[73] Bouckaert I, Godio M, Pacheco de Almeida J. Modeling of frames with HybriDFEM, a pseudo-discrete-finite element model including nonlinear geometric effects and nonlinear materials. In: 9th ECCOMAS thematic conference on computational methods in structural dynamics and earthquake engineering. 2023.

[74] de Borst R, Crisfield MA, Remmers JJC, Verhausel CV. Non-linear finite element analysis of solids and structures. Wiley series in computational mechanics. 2nd ed.. Chichester; 2012, p. 527.

[75] Powell MJD. An efficient method for finding the minimum of a function of several variables without calculating derivatives. Comput J 1964;7(2):155–62. http://dx.doi.org/10.1093/comjnl/7.2.155.

[76] Meguro K, Tagel-Din H. Simulation of buckling and post-buckling behavior of structures using applied element method. Bulletin of Earthquake Resistant Structure, IIS, University of Tokyo 1999;32:125–35.

[77] Huang BZ, Atluri S. A simple method to follow post-buckling paths in finite element analysis. Comput Struct 1995;57(3):477–89. http://dx.doi.org/10.1016/0045-7949(94)00623-B.

[78] McGuire W, Gallagher RH, Ziemian RD. Matrix structural analysis. 2nd ed.. New York: Wiley; 2000.

[79] Crisfield MA. A consistent co-rotational formulation for non-linear, three-dimensional, beam-elements. Comput Methods Appl Mech Engrg 1990;81(2):131–50. http://dx.doi.org/10.1016/0045-7825(90)90106-V.

[80] Elkaranshawy HA, Elerian AAH, Hussien WI. A corotational formulation based on Hamilton's principle for geometrically nonlinear thin and thick planar beams and frames. Math Probl Eng 2018;2018(1):2670462. http://dx.doi.org/10.1155/2018/2670462.

[81] Borković A, Marussig B, Radenković G. Geometrically exact static isogeometric analysis of an arbitrarily curved spatial Bernoulli–Euler beam. Comput Methods Appl Mech Engrg 2022;390:114447. http://dx.doi.org/10.1016/j.cma.2021.114447, URL: https://www.sciencedirect.com/science/article/pii/S0045782521006794.

[82] Melchor-Placencia C, Málaga-Chuquitaype C. A nonlinear modelling framework for unbonded post-tensioned timber members. Structures 2024;59:105715. http://dx.doi.org/10.1016/j.istruc.2023.105715, URL: https://www.sciencedirect.com/science/article/pii/S2352012423018039.

[83] Gan BS, Huong TT, Kien ND. Post-buckling behaviour of axially FGM planar beams and frames. Procedia Eng 2017;171:147–58. http://dx.doi.org/10.1016/j.proeng.2017.01.321.

[84] Di Re P, Addessi D, Gatta C, Parente L, Sacco E. Corotational force-based beam finite element with rigid joint offsets for 3D framed structures. Comput Methods Appl Mech Engrg 2024;419:116656. http://dx.doi.org/10.1016/j.cma.2023.116656, URL: https://www.sciencedirect.com/science/article/pii/S004578252300779X.

[85] Machado ICV, Viana HF, da Silva RGL, Costa RS, Lavall ACC. Finite element model for advanced analysis of plane steel frames with hinged end conditions including von Mises criterion. Structures 2022;46:1918–37. http://dx.doi.org/10.1016/j.istruc.2022.10.116, URL: https://www.sciencedirect.com/science/article/pii/S235201242201013X.

[86] Dubois F, Acary V, Jean M. The Contact Dynamics method: A nonsmooth story. C R Mec 2018;346(3):247–62. http://dx.doi.org/10.1016/j.crme.2017.12.009.

[87] Welzl E. Smallest enclosing disks (balls and ellipsoids). In: New results and new trends in computer science: Graz, Austria, June 20–21, 1991 Proceedings. Springer; 2005, p. 359–70.

[88] Godio M, Stefanou I, Sab K. Effects of the dilatancy of joints and of the size of the building blocks on the mechanical behavior of masonry structures. Meccanica 2018;53(7):1629–43. http://dx.doi.org/10.1007/s11012-017-0688-z.

[89] Portioli F, Cascini L. Contact dynamics of masonry block structures using mathematical programming. J Earthq Eng 2018;22(1):94–125. http://dx.doi.org/10.1080/13632469.2016.1217801.

[90] Desplanques Y. Amontons-Coulomb friction laws, A review of the original manuscript. SAE Int J Mater Manuf 2015;8(1):98–103, ISSN: 19463979, 19463987.

[91] Timoshenko SP, Gere JM, Prager W. Theory of elastic stability, 2nd ed.. Journal of applied mechanics, vol. 29, 1962, p. 220–1.

[92] Gere JM, Timoshenko SP, Saunders H. Mechanics of materials. 2nd ed.. J Vib Acoust-Trans ASME 1986;108:483–4.

[93] Simo J, Hughes T. Computational inelasticity. Interdisciplinary applied mathematics, vol. 7, New York: Springer; 1998, http://dx.doi.org/10.1007/b98904.

[94] Davis R, Henshell RD, Warburton GB. A Timoshenko beam element. J Sound Vib 1972;22(4):475–87. http://dx.doi.org/10.1016/0022-460X(72)90457-9.

[95] Meriggi P, de Felice G, De Santis S, Gobbin F, Mordanova A, Pantò B. Distinct element modelling of masonry walls under out-of-plane seismic loading. Int J Archit Herit 2019;13(7):1110–23. http://dx.doi.org/10.1080/15583058.2019.1615152.

[96] Gobbin F, de Felice G, Lemos JV. Numerical procedures for the analysis of collapse mechanisms of masonry structures using discrete element modelling. Eng Struct 2021;246:113047. http://dx.doi.org/10.1016/j.engstruct.2021.113047.

[97] Giordano A, De Luca A, Mele E, Romano A. A simple formula for predicting the horizontal capacity of masonry portal frames. Eng Struct 2007;29(9):2109–23. http://dx.doi.org/10.1016/j.engstruct.2006.10.011.